IMAGING L-ALANINE AND INOSINE INDUCED GERMINATION OF *BACILLUS ANTHRACIS* USING ATOMIC FORCE MICROSCOPY

An Major Qualifying Project submitted to the faculty of Worcester Polytechnic Institute in partial fulfillment of the requirements for the Degree of Bachelor of Science

Eric Michael Connelly

Advised by:
Professor Terri A. Camesano

April 30, 2009

Imaging L-Alanine and Inosine Induced Germination of *Bacillus anthracis* Using Atomic Force Microscopy

A Major Qualifying Project
submitted to the Faculty of
WORCESTER POLYTECHNIC INSTITUTE
Professors Terri A. Camesano, Advisor
by

_____
Eric Michael Connelly

April 30, 2009

Approval:

_____
Terri A. Camesano, Advisor

ABSTRACT

The goal of this project was to study the effects of germinants L-alanine and inosine on the morphology of *Bacillus anthracis* spores *in vitro* using atomic force microscopy (AFM) and phase contrast microscopy. Spores were incubated for four hours with germinants, deposited on mica, dried, and imaged in air. Spores exposed to inosine, L-alanine, and a combination of both germinants swelled to 2.0, 6.0, and 2.5 times the size (area) of the control spores respectively. However, only the sample that was exposed to both germinants entered phase-1 germination, turning phase-dark as studied by phase contrast microscopy. Bumps and ridges on the spore surfaces became far less prevalent and prominent in samples exposed to germinants.

ACKNOWLEDGEMENTS

I would like to thank my project advisor, Professor Terri A. Camesano, Department of Chemical Engineering at Worcester Polytechnic Institute, for providing this research opportunity and her mentorship. I would also like to thank Professor Camesano's graduate students Paola Pinzon-Arango, Joshua Strauss, and Sena Ada for providing expertise and mentorship throughout the project.

TABLE OF CONTENTS

LIST OF TABLES

LIST OF FIGURES

1. INTRODUCTION

Bacillus anthracis is the endospore-forming, etiological agent of the famous and deadly disease Anthrax. It is well known for its role in the 2001 terrorist attacks on the United States Postal Service distribution centers where 22 were infected (Fennelly, Davidow, Miller, Connell, & Ellner, 2004); however, *B. anthracis* is a naturally occurring microorganism and has a history of infecting and killing humans through more natural means as well. Humans may become infected by consuming undercooked meats of infected animals or through handling hair or hide of infected animals. Infections vary by type of exposure and include cutaneous, gastro-intestinal, and inhalational Anthrax. Inhalational Anthrax, which is caused by inhaling *B. anthracis* spores, is the target infection of terrorist attacks and results in nearly 100% mortality if the infection if left untreated (Centers for Disease Control and Prevention, 2001).

Besides *B. anthracis*, endospore-forming pathogens, including but not limited to *Bacillus* and *Clostridium* spores, threaten food safety in industrial and residential environments because of their resistance to high temperatures and chemicals and ability to adhere to surfaces such as pipes and containers. *Clostridum perfringens* will flourish in insufficiently cooled and heated food and can produce more than enough toxin necessary to give a person food poisoning. *Bacillus cereus*, a bacteria found in the guts of cows as well as in soil, is prevalent in cow's milk because of soiling of the udders, is extremely difficult to remove through pasteurization, and is capable or growing in temperature as low as 4ºC (Andersson, Ronner, & Granum, 1995). Knowledge of endospore morphology and behavior may yield new technologies that will protect public health and safety.

Prior studies have investigated the morphological changes of germinating *Bacillus atrophaeus*, *Bacillus anthracis sterne*, and *Bacillus subtilis* using atomic force microscopy (Chada, Sanstad, Wang, & Driks, 2003) (Plomp, Leighton, Wheeler, Hill, & Malkin, 2007) (Zaman, et al., 2005). They provide a preliminary understanding of Bacillus spore morphology and how Bacillus spore coats are shed during germination. This study is the first to compare spore morphologies under several germinant conditions using atomic force

microscopy and is an early step in understanding the mechanisms of spore germination. It also investigates whether germination proceeds more quickly in the presence of two germinants than in the presence of one. Knowledge of these mechanisms is critical to developing sanitation, disease control, and cell development theory.

2. BACKGROUND

2.1. GENUS *BACILLUS*

The genus *Bacillus* is a group of Gram-positive, endospore-forming, aerobic bacteria. The organisms within this genus vary widely in physiology, but all have the common ability to form protective spore coats and exosporium during periods when available nutrients are insufficient for growth and reproduction (Todar, 2004). *Bacillus* spores are able to survive extreme temperatures and harsh chemical environments for long periods (Gould, 1977).

2.1.1. SIGNIFICANCE

Bacillus anthracis, the causative bacteria of Anthrax, and *Bacillus cereus*, a common suspect for food poisoning, are the most medically important species. *B. anthracis* was the first microorganism proven to cause a specific human disease. Many other *Bacillus* species are being found to be prevalent human pathogens (Todar, 2004).

Despite their negative reputation as pathogens of insects, animals, and humans, *Bacillus* bacteria play an important environmental role. They are considered "normal flora" of soil and thought to be important players in degradation of biopolymers and Earth's nitrogen and carbon cycles. (Todar, 2004).

2.1.2. SPORE MORPHOLOGIES

B. anthracis spores can range in size from spherical cells approximately 0.8-0.9 μm in diameter (Zaman, et al., 2005) to elongated spores approximately 1.35 μm long and 0.75 μm wide (Chada, Sanstad, Wang, & Driks, 2003). Chada classified the elongated spores into two separate groups. The slightly smaller spores, measuring approximately 1.27 μm long and 0.74 μm wide, do not posses ridges and instead have bumps ranging between 8 and 40 nm in diameter. The larger spores, measuring approximately 1.47 μm long and 0.76 μm wide, have bumps and ridges. It is believed that the smaller group of spore still possessed their exosporium (Wang, Krishnamurthy, Jeong, Driks, Mehta, & Gingras, 2007), while the larger ridged spores had lost their exosporium "during culturing or preparation for AFM analysis"

(Chada, Sanstad, Wang, & Driks, 2003). The shed exosporium often appears as thin films adhered to the imaging surface surrounding spores in atomic force microscopy images (Plomp, Leighton, Wheeler, & Malkin, 2005), as shown in Figure 1. It is unknown why Chada had not seen spherical cells in his studies or why Zaman did not mention the visible elongated cell in Figure 1(a) in his paper.

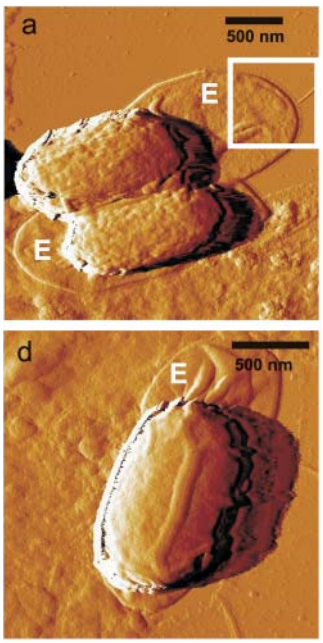

FIGURE 1 – AFM IMAGE OF BACILLUS ATROPHAEUS EXOSPORIUM LABELED "E" (PLOMP, LEIGHTON, WHEELER, & MALKIN, 2005)

2.1.3. GERMINATION

When nutrient-rich conditions return to the Bacillus spores, they lose their protective exosporium and spore coats and thus become vulnerable to their environment. The cells must be sure that the environmental conditions are conducive to growth and reproduction before they germinate. The signals that trigger this response are small molecules and ions called germinants. These various germinants can signal Bacillus cells, without any other environmental inputs, to germinate out of their dormancy and into a vegetative state (Paidhungat & Setlow, 1999).

Early spore germination is considered a strictly biophysical process because spores have no metabolism or mass transfer during their dormancy. Germination is carried out by enzymatic processes that first degrade the spore coat. The inner germinant receptors are then exposed and activated, restarting the cell metabolism. Germination occurring without enzymatic germinants proceeds slowly in comparison (Moir A. , 2006). Based on an isobaric protein tagging system carried out at the University of Michigan, degradation of several outer protein layers of *Bacillus anthracis* occurred within 17 minutes of initial exposure to Difco Sporulation Media, which contains enzymatic germinants. During this period the cells were still in a dormant state and had not restarted their metabolic processes. Within the next 20 minutes, cells showed a modest increase in proteins known to be involved in key metabolic processes (Jagtap, et al., 2006). It is expected that germination would occur quickly since rapid outgrowth would help the cells compete with other species in environments where nutrients come and go quickly.

Marco Plomp, an experienced researcher of Bacillus spore germination, most recently released high-resolution atomic force microscope images of the germination of *Bacillus atrophaeus* using 100 mM L-alanine, 1.65 mM L-Asparagine, 2.8 mM D-Glucose, 2.8 mM D-Fructose, 5 mM potassium chloride, and 25 mM Tris HCl buffer pH 8.0. These images revealed de-evolution of *B. atrophaeus*'s complex rodlet spore coat layer. He found that within 13 minutes, "etch pits" as deep as 70 nm were formed. These pits initiated larger fissures that formed perpendicular to the organized rodlet layer and expanded in both axes as the vegetative cell emerged. The fissures expanded more rapidly around imperfect stacking faults of the rodlet structure. The first signs of expansion appeared at 5:45 (in hr:min). Vegetative cell emergence did not occur until after the 8 hour imaging period. Plomp also found that in his studied conditions spores turned phase-dark after just 15 minutes, which corresponded to the initiation of phase-1 germination (Plomp, Leighton, Wheeler, Hill, & Malkin, 2007).

Esterase activity (EA) may provide a benchmark for measuring germination of Bacillus spores because EA is associated with activation of proteases and cortexlytic enzymes, which are essential to early stage, Phase-1 (pre-metabolism) germination. The EA for *B. anthracis*

after exposure to both L-alanine and inosine is 100 times larger than the EA with either sole germinant (Ferencko, Cote, & Rotmana, 2004). This raises the question of whether the combination of these germinants accelerates the germination process.

2.2. Atomic Force Microscopy

2.2.1. Fundamentals

Atomic force microscopy is rather different than traditional imaging technologies. Instead of measuring light, directly by the operator's eye or by a photodiode, an AFM measures a surface by touch. The modern tip that is used as a measurement device is a silicon chip with an attached thin, flexible microcantilever. On the end of this cantilever is a tip that can range from a 1 um or larger tip, which is typically used for force measurements, to a thin carbon nanotube, which provides high-resolution images.

During imaging a laser is shone onto the cantilever where it is reflected onto a photodiode. After proper calibration, the relative position of the cantilever correlates to the laser position on the photodiode. Normal vertical deflection of the cantilever translates into a vertical deflection of the laser onto the receiving photodiode, while torsional cantilever deflection translates into horizontal laser deflection. These two datum are combined to give three dimensional topography of the sample.

Three modes exist for measuring samples. In contact mode, the cantilever force sensor is placed on the sample and dragged across the surface. This method provides topographical data only, and is slightly less accurate than the second and third method, tapping and non-contact modes.

In tapping mode, the cantilever is directly vibrated using a small electrostatic device at the cantilever's resonance frequency and the desired drive amplitude. The cantilever is brought to immediately above the sample where it is scanned across the surface. The tip of the cantilever gently taps the surface at the bottom of each phase of the tip's vibrations, thereby changing the amplitude and phase of the cantilever vibration. As the tip scans the surface, the height of the tip is adjusted using a piezoelectric element to keep the amplitude

of the cantilever at the desired amplitude set-point. Proper control of the cantilever height is achieved using a feedback loop with proportional and integral corrections.

Tapping mode is gentler on the sample because there is much less direct contact between the tip and the sample, however and even more gentle method exists. In non-contact mode the cantilever is also vibrated much like in tapping mode; however, during non-contact mode, the amplitude of the cantilever is made small enough that it can measure the strong repulsive and attractive intermolecular forces between the cantilever tip and sample. In this mode the topography of the sample may be taken without disturbing the surface of the sample since it does not rely on contact between the tip and sample.

Three images may be derived from tapping mode, the mode used in this study. The first is a height image, or a topographical image. The second is a map of the force applied to the cantilever tip each time it contacts the surface of the sample, which is calculated using the amplitude data. The third image represents the difference between the phase of driving element and the phase of the cantilever. Only height images may be used for quantitative analysis. Amplitude and phase images may only be used for qualitative analysis because they contain no direct measurements of the surface topography.

3. METHODOLOGY

Four groups of *B. anthracis* were examined using atomic force spectroscopy and phase contrast microscopy after incubation in the following conditions:

TABLE 1 - GERMINANT CONDITIONS

	L-Alanine	***Inosine***	***Tris-Hcl pH 7.0***
Control	0	0	0
Sample 1	50.0mM	0	25.0mM
Sample 2	0	5.0mM	10.0mM
Sample 3	50.0mM	5.0mM	17.5mM

The following flow chart (Figure 2) shows the steps taken during this study:

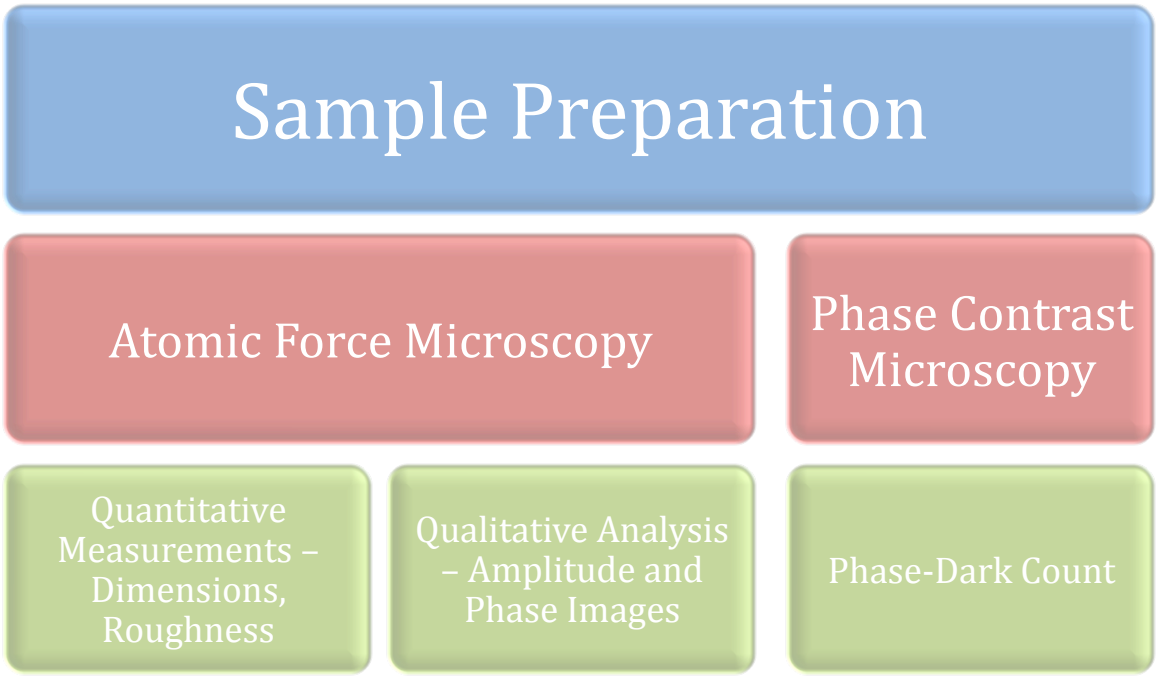

FIGURE 2 – METHODOLOGY FLOW CHART

3.1. SAMPLE PREPARATION

For each sample, stock *B. anthracis* was combined with the germinant solutions in a micro-centrifuge tube. Samples with germinants were incubated for 4 hours at 37 °C while being inverted at 40 rpm. The cells were spun down at 5000 rpm for 4 minutes and washed with double-distilled water three times. They were then re-suspended in the original volume of water. All samples were then sonicated for 10 minutes in a Branson 1510 sonicator. Two ten µL volumes of each suspension were transferred to two separate slides of freshly cleaved mica taped to glass slides. One slide was left to settle for 10 minutes and then briefly (3 seconds) rinsed with double-distilled water. Both slides were then left to dry for at least 24 hours. The rinsed slide aided in imaging single, lone cells.

3.2. ATOMIC FORCE MICROSCOPY

The atomic force microscope used for these images was a Veeco (Digital Instruments) Dimension 3100. A Digital Instruments isolation barrier was also installed around the AFM. Tips used were MikroMasch Ultrasharp NSC15/AIBS, a single-cantilever, general-use tip. The air in the instrument room was kept below 15% relative humidity.

3.2.1. SET-UP

Overall, set-up and operation of the AFM was fairly simple; however, adjusting and tuning the AFM was critical in obtaining accurate, detailed images. An AFM tip was installed on a dry, clean tip holder, and the tip holder was installed onto the AFM laser. The laser unit was removed from its cradle and turned so the laser cast onto a surface. The laser was aligned onto the cantilever by first turning the right knob on the top of the laser clockwise until the laser spot vanished from the surface, and then slowly turned back to counterclockwise until the spot was fully visible again. This adjustment aligned the laser horizontally on the tip; the disappearance of the spot corresponded to the tip body obstructing the laser. Next the cantilever was aligned vertically using the top left knob. The knob was adjusted until the dot suddenly disappeared and then reappeared. This behavior corresponds

to the laser hitting and reflecting off of the thin cantilever for an instant as the laser passed over it. If the laser spot gradually disappeared, it meant that the tip was installed crooked and required adjustment. Once the cantilever was found, the laser was adjusted to reflect off of the vertical center of the cantilever to obtain maximum 'sum' as seen on the computer and then adjusted horizontally to obtain the maximum 'sum' while still casting close to the end of the cantilever. The laser unit was then reinstalled and locked into the AFM.

The next step was to adjust the photodiode to center the laser upon it. This was accomplished by adjusting the knobs on the left side of the laser. The upper knob moved the laser on the x-axis and the lower knob moved the laser on the y-axis. First, the laser dot on the laser objective was moved to the rough center of the window. Finally, the computer objective was observed to finely tune the photodiode. The final desired outcome was to have a dot touching the crosshairs of the computer objective and have a deflection less than 1.0.

At this point the AFM was ready for calibration of the cantilever resonance. This step was completed before any of the proceeding steps because resonance was often not acceptable and the only way to adjust the resonance properties of the cantilever was to move slightly the tip body in the tip holder, thereby undoing all laser and photodiode alignment. To begin oscillations, 'Z modulation', 'amplitude setpoint', and 'drive amplitude' were set to 1, 2 V, and 300 mV respectively. The tuning fork icon was selected to begin tuning. A new window opened, which displayed drive settings and a chart of the resonance amplitude versus the resonance frequency. To achieve this data, the controllers completed 'sweeps' of frequencies within the specified sweep range. The easiest method for calibration was to set the 'peak offset' to 10 percent, set the 'sweep range' from about half the tip-manufacturer's resonance specification to about twice the value, and then by click auto-tune function. After a successful automatic tune (where an obvious lone, offset peak was observed) the amplitude setpoint was adjusted to 2.0 V and drive amplitude was increased until the maximum amplitude value reached to at least half the height of the graph. The maximum acceptable drive amplitude was 600 mV. If this value was reached before the amplitude reached half the height of the graph, the laser was inverted, tip holder removed, and tip slightly adjusted in the tip holder. Even small adjustments of the tip would result in better (or worse) cantilever

resonance. Re-centering of the laser and photo-diode were required after any adjustment to the tip.

If quality phase images were desired, it was important to NOT change the phase after auto-tune was performed. The program tunes the phase of the cantilever before it offsets the peak. This method provided very good quality phase images.

After the cantilever was tuned, the AFM optics were centered and focused onto the cantilever. The 'Locate Tip' button (magnifying glass with yellow tip) was first pressed to focus on the cantilever. A window with a real-time microscope image appeared. Using this image as a guide, the focus was adjusted using the track ball and the pan was adjusted using the two knobs on the AFM optics. The desired outcome was to have the cantilever in focus with the crosshairs centered at the approximate location of the tip.

After adjusting the optics, the cantilever was lowered to the surface of the sample and engaged. This was done by first focusing the optics on the surface by lowering the cantilever using the 'Focus Surface' button. When the small white dots of the cells were visible but not quite in focus, the 'Focus Surface' window was exited. The scan size was set to a value between 2.5 and 10.0 um and the tip was engaged using the 'engage' command. The tip first jumped down to the start position and then was incrementally lowered. During lowering the z-value on the very bottom of the screen was watched. If this value did not increase before engaging, it was considered a false engage. Rarely a false engage, caused by high humidity or controller error, was fixed by simply disengaging the surface and re-engaging.

3.2.2. IMAGE TUNING

Typically after engaging the surface, the computer increased the amplitude set-point to the point that it would disengage the surface. It was therefore necessary to reduce the amplitude set-point back to a value of 2.0. This was usually enough the re-engage the surface; however, if the tip had still not re-engaged the surface (the tip position read 'retracted'), then the drive amplitude was slowly increased until the tip tracked the surface accurately.

The image size was then adjusted to 20 µm. X- and Y- axis were varied to scan along the surface of the sample until an object with a height of at least 0.3 µm was found. The object was then centered in the scope and the image size was decreased to 10 µm, 5 µm, and then 2.5 µm. The image was then tuned by adjusting the proportional and integral gains. Proportional gains had the smaller effect on image quality, but if too high, the proportional gain would cause low frequency noise in the image. Typical proportional gains ranged from 1.2 to 2.0. The integral gain was first increased until high frequency noise was obvious, and then decreased until little noise was apparent. Since high control-loop gains provided more accurate tracking of the tip and higher quality amplitude and phase images, an image with a little edge noise was deemed acceptable. It was not a goal to completely eliminate noise, since noise at the edges of the cells could only be eliminated with an accompanying reduction in image quality caused by less accurate tracking.

Images were captured at 1.0 Hertz, 512 points, and 512 lines. A variety of scan sizes were used to provide images for size and image calculations as well as qualitative analysis.

3.2.3. Image Analysis

The goal of image analysis was to measure cell length, width, height, and roughness for each condition. Qualitative observations were also made using the amplitude and phase images.

Height images were first selected using the ‘Image’ pull-down menu and selecting either ‘Select First Image’ or ‘Select Left Image’. After an image was selected, ‘Analyze’ and ‘Modify’ pull-down menus appeared. The image was flattened using the ‘Plane Fit Auto’ tool under the ‘Modify’ menu’. This function was used rather than the ‘Flatten’ tool because ‘Plane Fit Auto’ has the ability to adjust the entire image based on a correction derived from sections of the mica surface. In contrast, ‘Flatten’ looks at each data line individually and adjusts the tilt and height accordingly. ‘Flatten’ does not differentiate between cell and mica, which leads to incorrect correction and the formation artifact image structures.

To flatten the image the ‘Plane Fit Auto’ option was selected under the ‘Modify’ menu. After the dialog box appeared, section of bare mica were selected on the image by simply

clicking on the image and dragging the box to the correct size. A relatively small area if mica is required to flatten the image correctly, but in general several large areas were selected to guarantee an accurate correction. After the areas were selected, the 'XY' button in the dialog box was pressed to indicate that box x- and y-axis image corrections were required. 'Execute' was then pressed to complete the process and flatten the image.

Once the image was corrected for tilt and bow, cell measurements were taken. Cells were measured using the 'Section' tool under the 'Analyze' pull-down menu. The length of a cell was measured by drawing a bisecting line through the longest length of the cell. Lines were drawn by clicking once to initiate a line and then clicking a second time to terminate the line. After the line was drawn, a box appeared prompting the user to mark two locations with red arrows. The program used these two points to measure length, height differences, and several other parameters. To measure length or width the red flags were placed at the local minimum of the edges of the cell. Width was always measured using a line perpendicular to the original length line. Height was measured by drawing a line that bisects the approximate highest point on a cell and any patch of bare mica. One marker was placed on the maximum height of the cell and the second on bare mica. For cells that had obvious edge artifacts caused by very abrupt height differences, the edge markers were placed at the approximate edge of the cell, guided by the visual image on the screen, rather than the absolute end of the cell. This method allowed for better comparison of cells that were grouped together and had no abrupt height changes to lone cells that displayed some image artifacts.

Once the cells' dimensions were recorded, the root mean square (RMS) roughness of the cells was measured using the 'Roughness' tool in the 'Analyze' pull-down menu. No matter the image scan size, a 371 nm by 371 nm box was drawn on the cell near the area of maximum height. Sometimes multiple, non-overlapping reading were taken if cells were large and relatively flat and then averaged. Measurements were never taken near cell edges because the RMS roughness calculation method is a height-difference calculation. Measuring on an edge would misrepresent the actual roughness.

3.3. PHASE CONTRAST MICROSCOPY

Phase contrast microscopy was the benchmark for determining the extent of germination of each *B. anthracis* sample. A Nikon Eclipse E400 phase contrast microscope was used with a 100x/1.30 Nikon Plan Flour oil immersion objective and a PH3 light filter. Images were acquired from the microscope using a Diagnostic Instruments Insight camera and the SPOTSoftware Advanced imaging application. All samples were prepared and imaged side-by-side to decrease variability. For this experiment, the control population was incubated in 50mM Tris-HCL alongside the other samples. This is an improvement over the control used for AFM because it decreased the variability between samples.

3.3.1. SLIDE PREPARATION

Ten µL of suspended, prepared sample from each condition was placed on a clean glass slide and topped with a cover slide. Samples were allowed to settle for at least 10 minutes to increase adherence of cells to the glass and reduce water movement during imaging.

3.3.2. PHASE CONTRAST IMAGING

One drop of oil was place on top of the cover slide. After image was visually acquired and focused, it was captured using SPOT advanced. The program's capture settings were set at gamma 1.0 and brightness 0.92.

4. RESULTS AND ANALYSIS

Data on cell length, width, height, and RMS roughness obtained via atomic force microscopy and images obtained via phase contrast microscopy were the two means for analysis in this study.

4.1. CONTROL SPORE SIZE

The first control image taken, as seen in Figure 3, was ideal for comparing our research specimen to Chada, Zaman, and Wang's specimens, which were reviewed in 2.1.2.

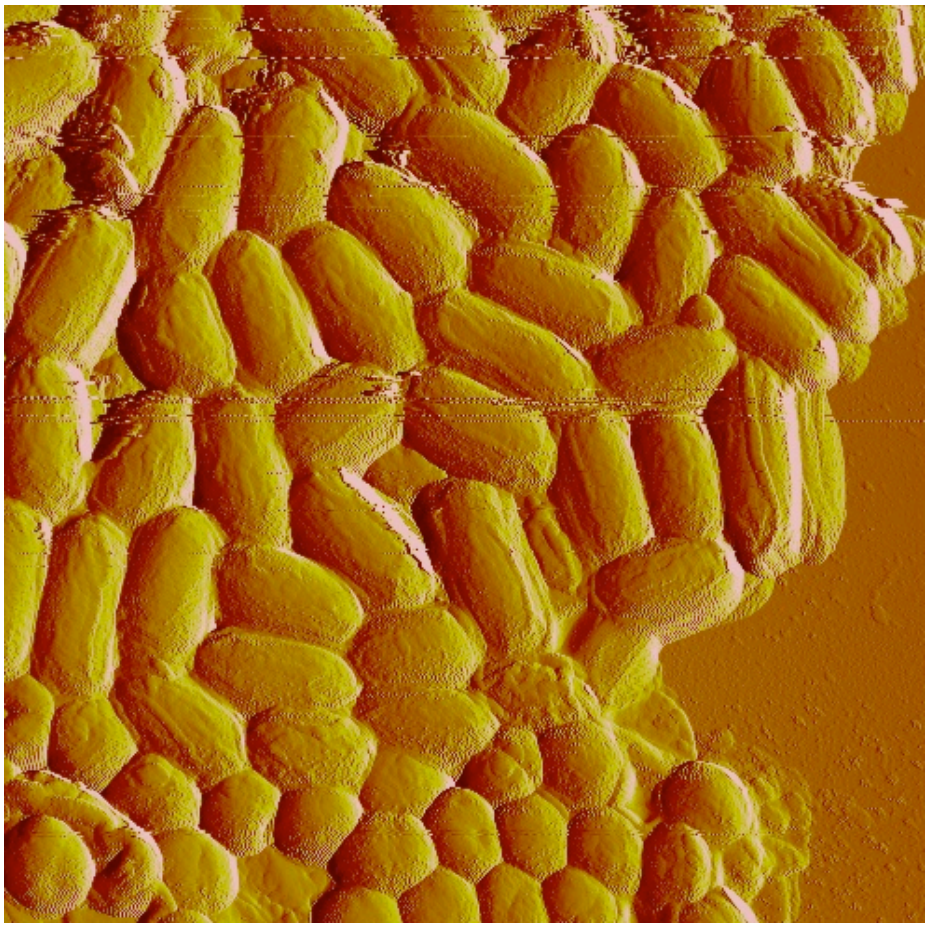

FIGURE 3 – AFM PHASE IMAGE 001, CONTROL 10µM SCAN SIZE

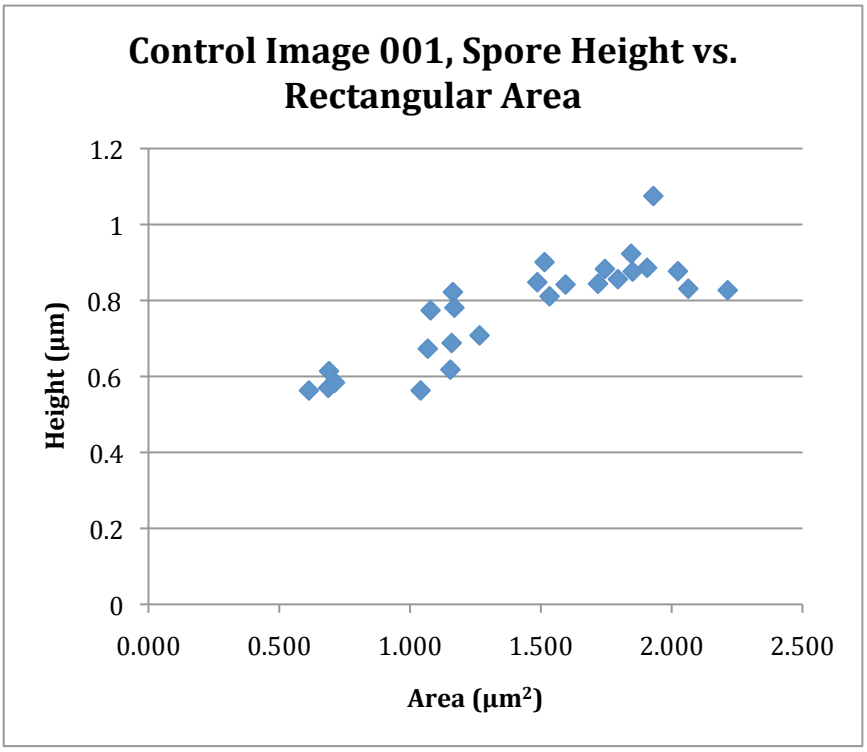

FIGURE 4 – CONTROL IMAGE 001, SPORE HEIGHT VS. LENGTH

In Figure 4, the heights of the cells were graphed against their rectangular areas (length times width). In this graph it is apparent that three separate groups of cells exist, being spherical, small elongated, and large elongated. This supports the findings of Zaman, who imaged spherical cells, and Chada who imaged elongated cells. Furthermore, Chada and Wang's hypotheses regarding exosporium and cell ridges are supported by the phase image in Figure 3. It is clear that the largest elongated cells, those that are predicted to have completely lost their exosporium, have large defined ridges; the medium sized elongated cells have bumps and small ridges; and the small spherical cells have smooth surfaces. It is important to realize that these 'roughness' observations are based on qualitative analysis of a phase image and not measurements of RMS roughness or ridge size based on height data, which is explained in section 4.3.

4.2. MORPHOLOGICAL CHANGES TO GERMINATION

Figure 5 represents the size of all measureable cells imaged during this study.

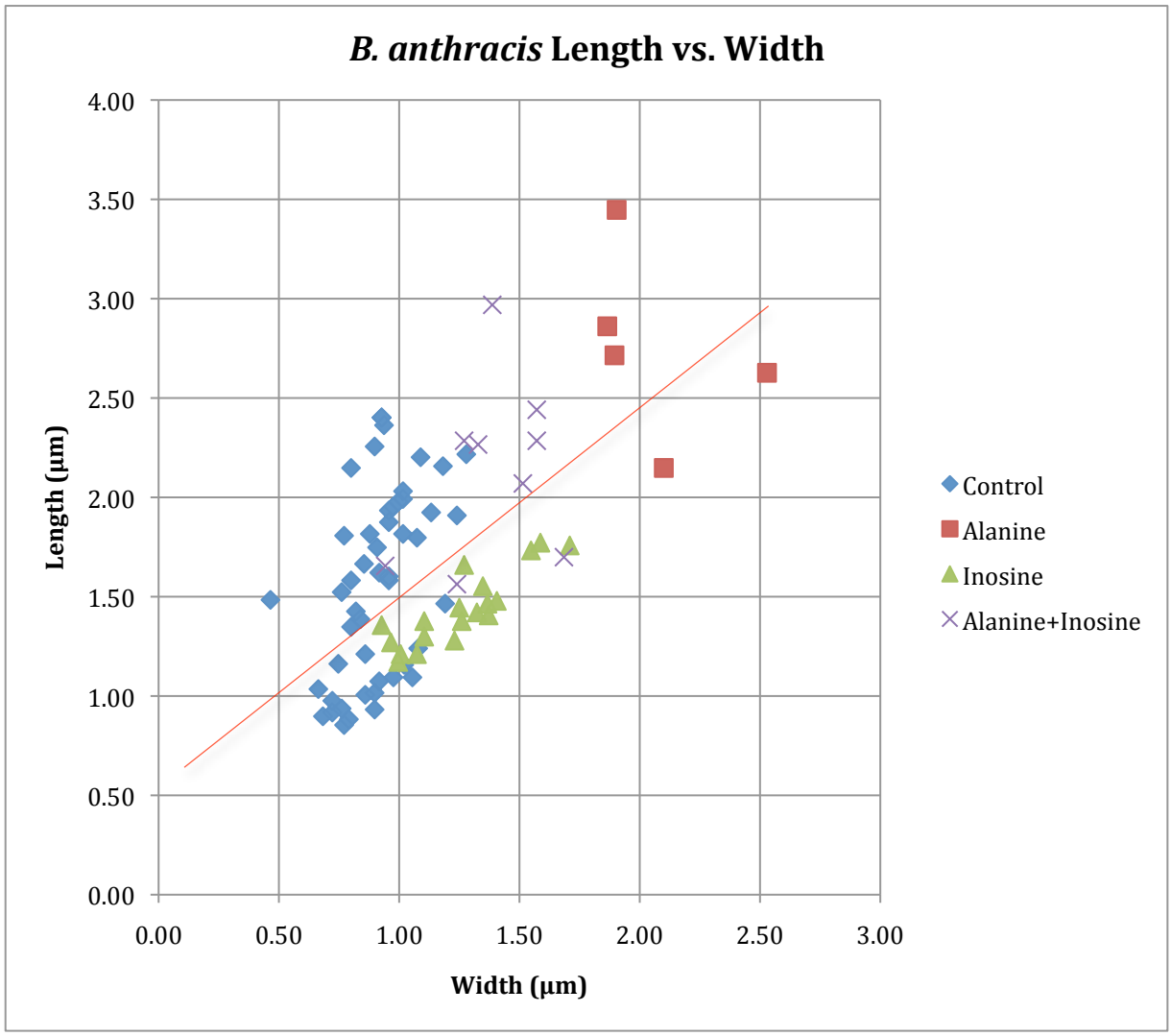

FIGURE 5 - *B. ANTHRACIS* LENGTH VS WIDTH

The red line in Figure 5 separates the spherical from the elongated spores. Notice that no elongated inosine spores were imaged. This does not mean that there were no elongated cells present. Elongated inosine spores were observed during phase contrast microscopy, which is

described later in section 4.3. It seemed during these experiments that the spherical cells were more common in the inner regions of the dried sample droplet and the elongated cells were more common on the outer regions. This may have to do with the difference in hydrophobicity based on the existence of the exosporium. It was not an objective to image both circular and elongated cells equally.

By separating the data into these two categories we may accurately measure the swelling of spores as they germinate. Figure 6 shows the range and average cell area for each spore subgroup.

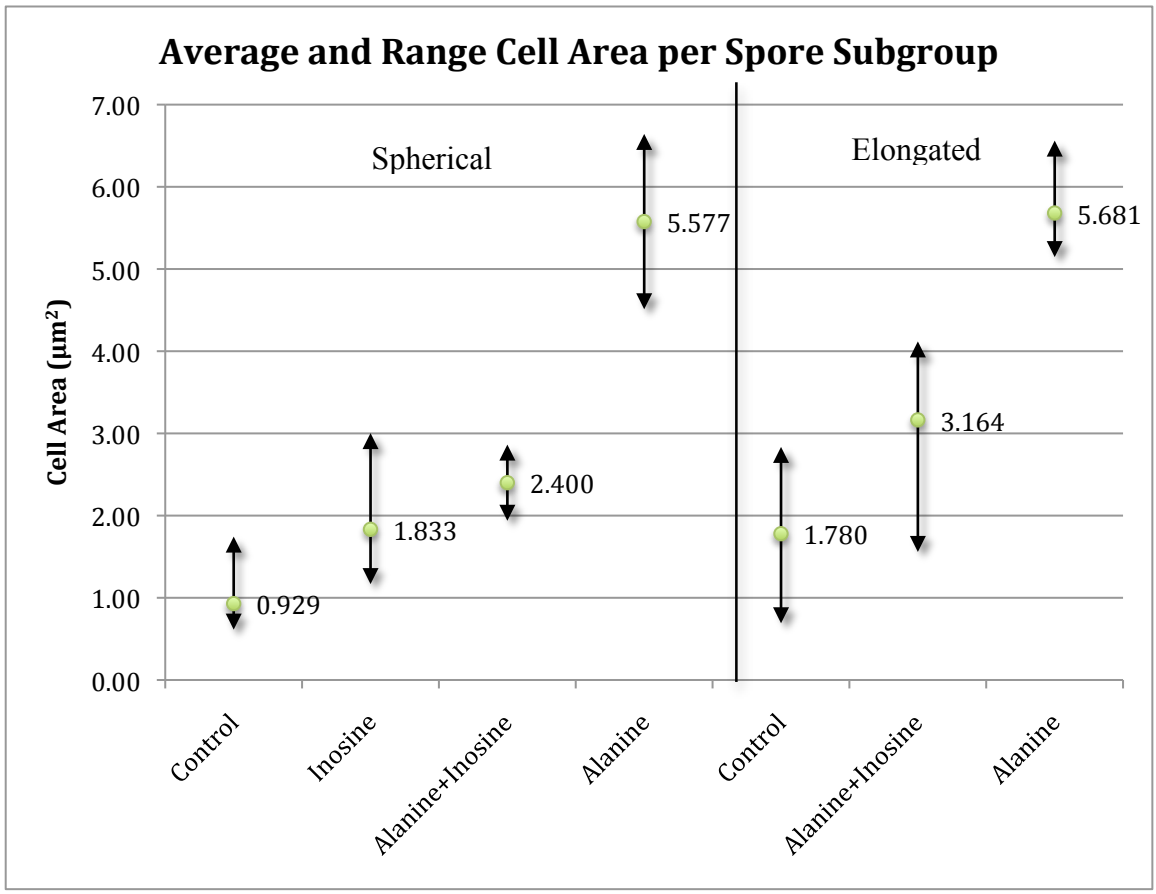

FIGURE 6 – AVERAGE AND RANCHE CELL AREA PER SPORE SUBGROUP

This data suggests that at least in the case of inosine and L-alanine, exposing spores to two germinants does not necessarily increase degradation of the spore coat, which corresponds to cell swelling. It is possible that spore became more swollen under exposure to

L-alanine alone than under exposure to both germinants because of some receptor site interference.

4.3. CELL ROUGHNESS

Two methods were used to evaluate cell roughness. The first was a quantitative method using and RMS roughness calculator on the NanoScope software. For each cell a 0.371x0.371 µm square section was selected on the height image of the cell. This area was never selected over an edge, noise, or any image artifact to ensure an accurate roughness measurement. The results are summarized below in Figure 7.

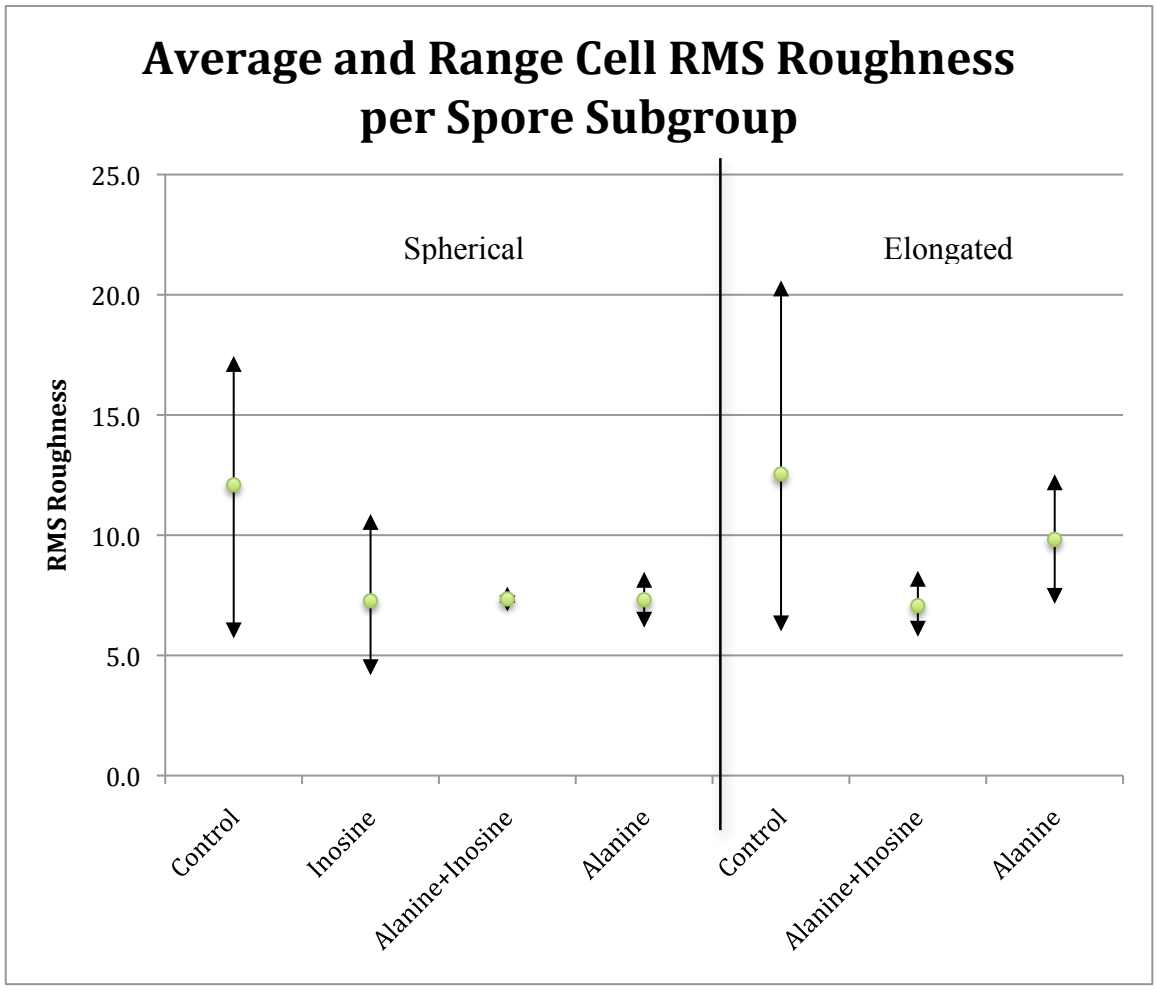

FIGURE 7 – AVERAGE AND RANGE CELL RMS ROUGHNESS PER SPORE SUBGROUP

Roughness measurements varied greatly throughout individual cells because of surface features like bumps and ridges. The average roughness of the control cells was higher than those of the germinant conditions but also had a very large range of roughness. Since far fewer L-alanine and L-alanine+inosine cells were imaged, it is quite possible that the narrower range of these groups was caused by a smaller sample. Overall, the quantitative roughness results were inconclusive. The surface roughness measured at this resolution is highly dependent on humidity, tip tracking, and AFM tuning.

The second method for analysis is a qualitative analysis based on the AFM phase images. The apparent surface structures of the cells were highly variable. Cells were often smooth, bumpy, ridged, and even highly wrinkled. The images in Figure 8 are a good representation of the surface structures of each sample. These images have been adjusted so that they represent equal scale. All cells in these images, except the right cell in the control image, are spherical cells, so the size difference between each sample may also be visually compared.

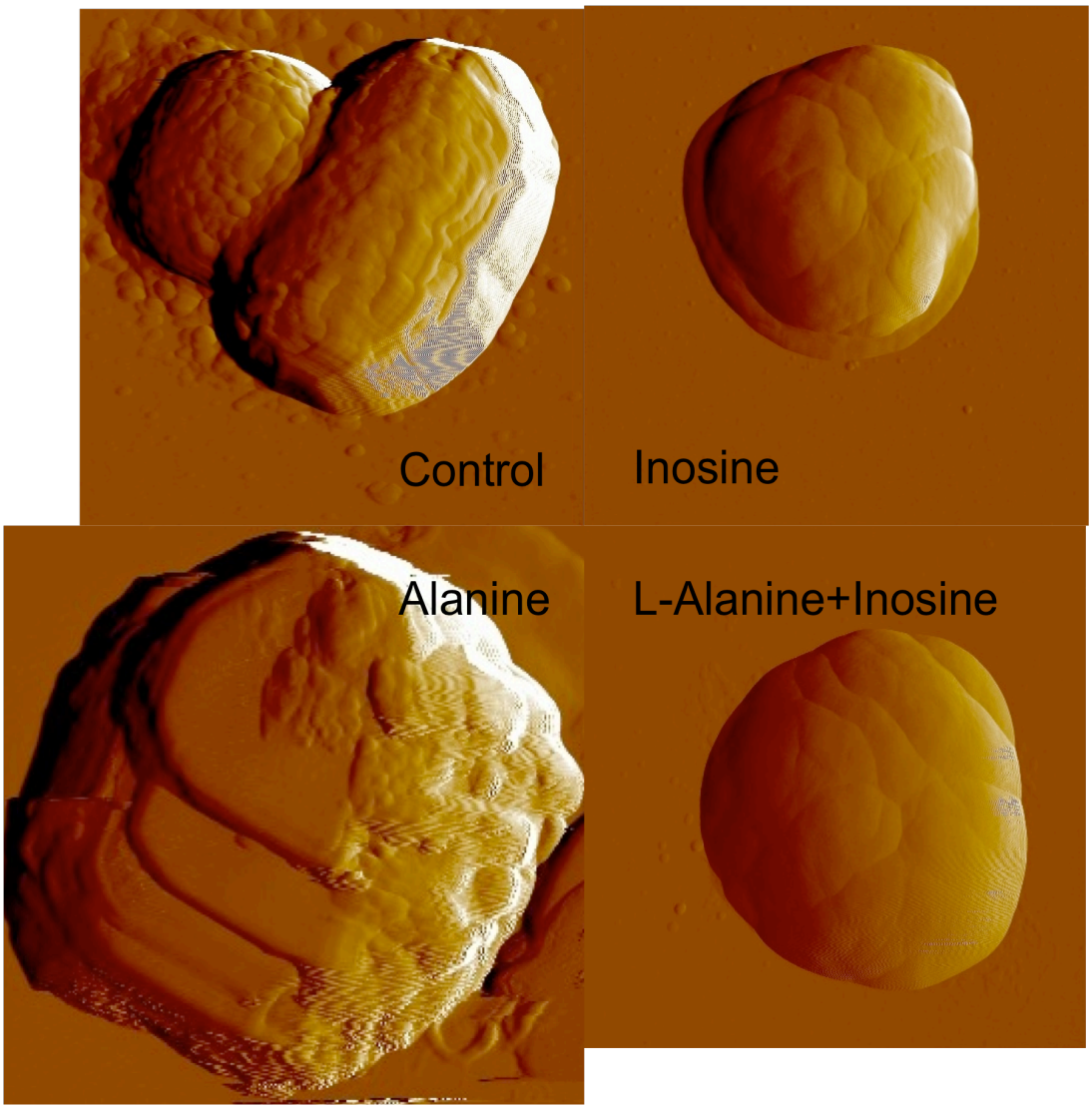

FIGURE 8 – SPORE COAT SURFACE STRUCTURE COMPARISON

You can see the bumpy and ridged structures in the two control spores. Smooth spherical cells were also found in the control as can be seen in Figure 3 or Appendix A. Inosine and L-alanine+inosine samples were often smooth. It is unclear whether these features are cause by AFM tuning and humidity or because they have began to absorb water and expand, which would 'stretch' the outer spore coat. Alanine cells were the most curiously shaped cells of this study. They seemed to have very smooth plateau-like surfaces with bumpy deposits, as if they were smooth but 'dirtied'. Their unusual surface structure and shape may be related to a

high amount of spore coat degradation and cell swelling without entering phase-1 germination, as described in the following section.

4.4. PHASE CONTRAST IMAGES

Phase imagery provided more predictable results than the AFM imagery and analysis. Figures 9, 10, 11, and 12 show phase contrast images of the control, inosine, L-alanine, and L-alanine+inosine samples respectively. All four of these samples were prepared side-by-side and imaged within the same 30-minute period.

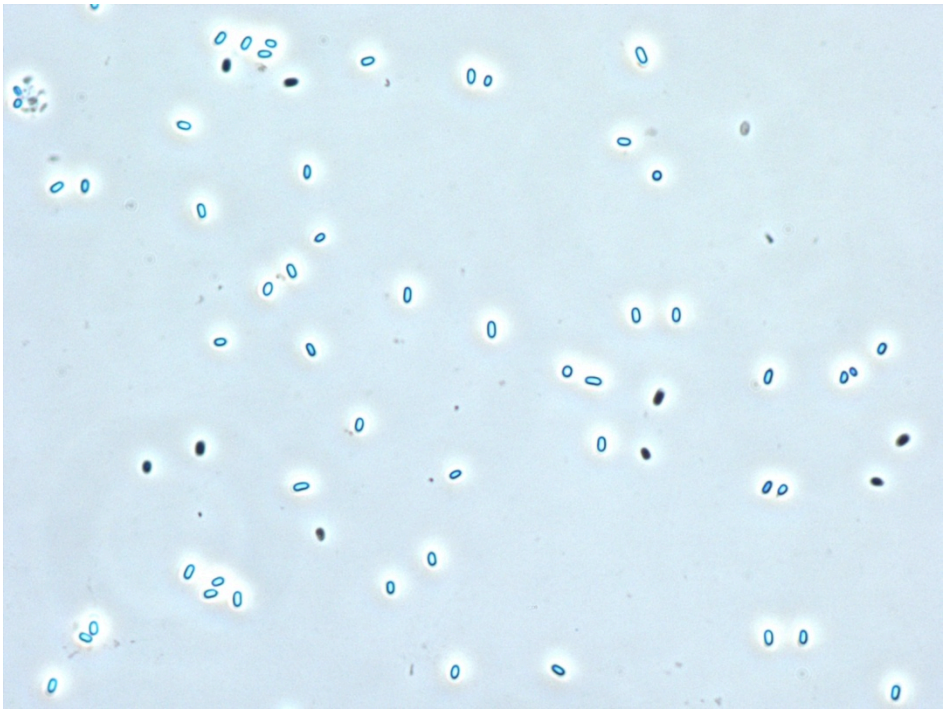

FIGURE 9 – PHASE CONTRAST IMAGE, CONTROL

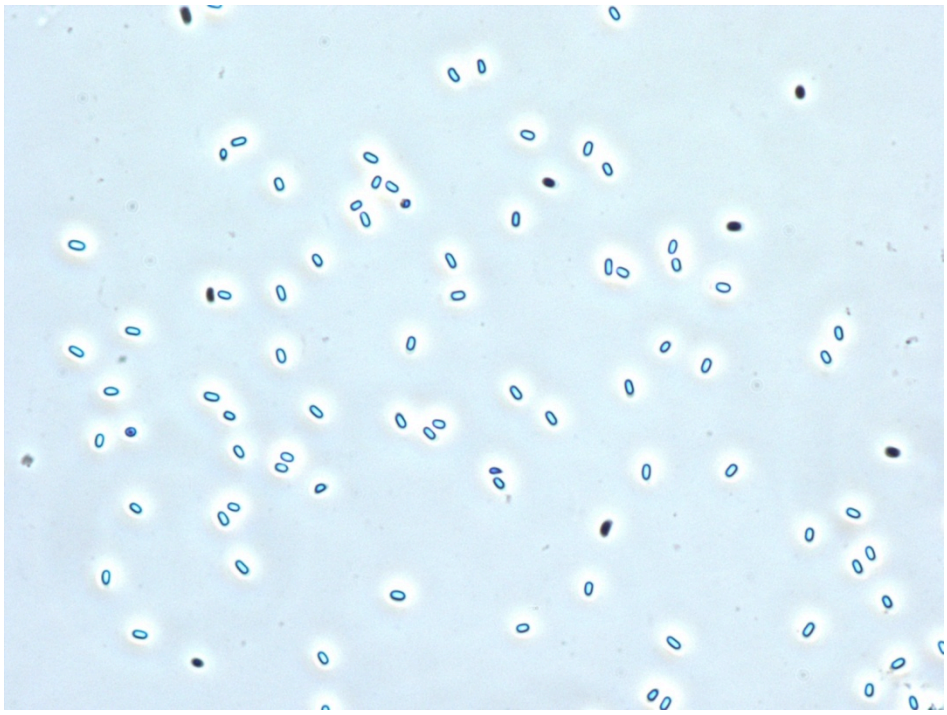

FIGURE 10 – PHASE CONTRAST IMAGE, INOSINE

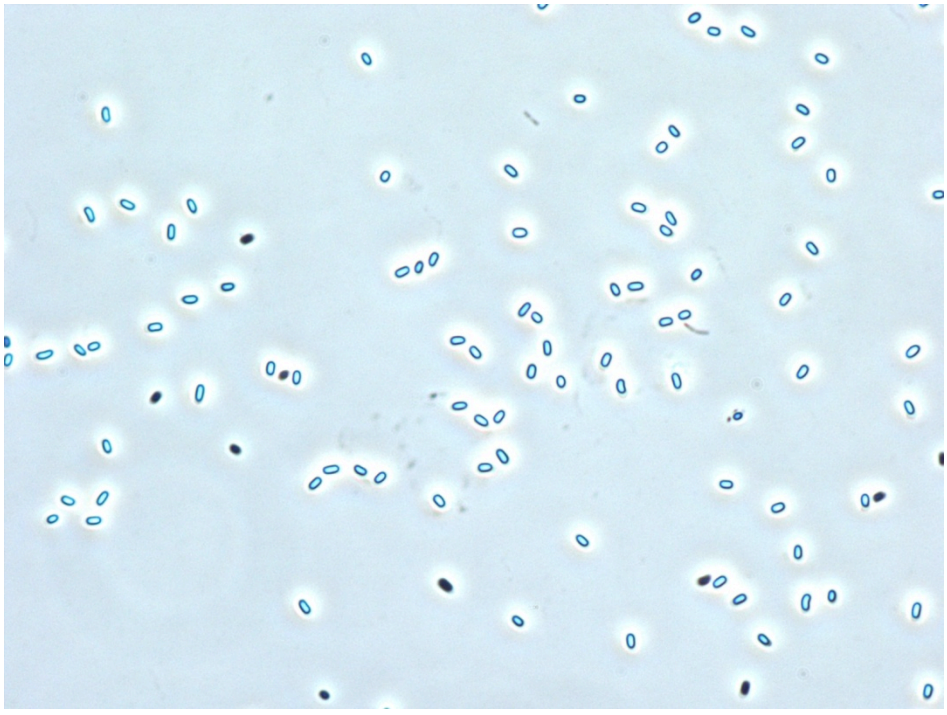

FIGURE 11 – PHASE CONTRAST IMAGE, L-ALANINE

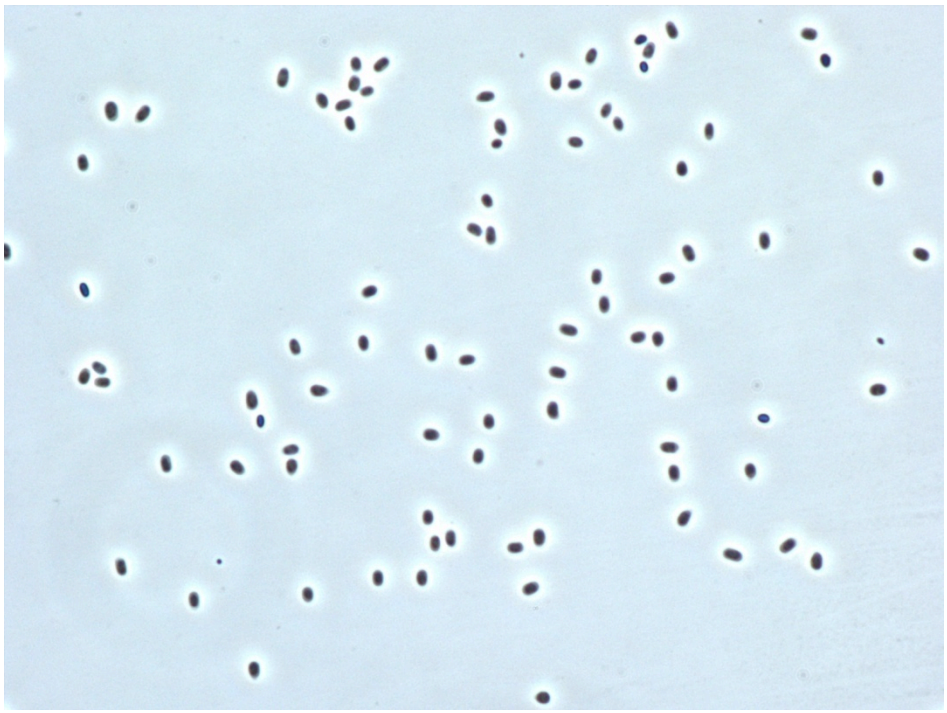

FIGURE 12 – PHASE CONTRAST IMAGE, L-ALANINE+INOSINE

The ‘germinated’ cells in the control sample are thought to be leftover cells from the sporulation/culturing process. During this process spores germinate, grow, and enter spore dormancy. If a spore does not undergo complete germination it could potentially withstand the washing process, which is completed to lyse fully vegetative cells. This theory is supported by this study’s results. If washing processes destroyed germinated spores, the spores would not show up in any of our samples.

The inosine and L-alanine samples did not show a substantial increase in phase-dark cells over the control sample. These samples did not enter phase-1 germination, which corresponds to the activation of proteases and cortexlytic enzymes. The L-alanine+inosine sample entered phase-1 germination because the vast majority of these cells turned phase-dark.

The increase in size of the germinant samples over the control can be attributed to spore coat degradation by the enzymatic properties of L-alanine and inosine. Even with the high amount of swelling (spore coat degradation) in the L-alanine sample, exposure to only one

germinant was not enough to activate phase-1 germination. This is supported by the EA study by Ferencko as explained in section 2.1.3.

It is unclear why the L-alanine sample showed much more growth than the L-alanine+inosine sample. One might predict that more germinants would cause more enzymatic activity and spore coat degredation. It is clear that inosine causes less swelling in *B. anthracis* than L-alanine. It is therefore possible that inosine interferes with L-alanine at the cell's receptor sites, where the degradation of the spore coat is triggered.

5. CONCLUSIONS AND RECOMMENDATIONS

From the size and germination data obtained from the AFM and phase contrast images we can conclude that L-alanine and inosine at the studied conditions cause B. Anthracis spores to swell but do not enter phase-1 germination. Also, L-alanine in combination with inosine germinates B. Anthracis spores but causes less spore swelling than L-alanine alone. This may be caused by interference by inosine at spore receptor sites where L-alanine would otherwise have full access to degrade the spore coat.

A quantitative roughness analysis of the spores was inconclusive because the AFM resolution was not detailed enough to capture the nano-scale structure changes associated with germination. At the recorded resolution, images and roughness were highly dependent on external factors such as humidity, tip tracking, and AFM tuning.

The shape of spores was highly variable. Surface structures varied and included smooth, bumpy, and ridged features. Bumps and ridges on the spore surfaces became far less prevalent and prominent in samples exposed to germinants.

5.1. RECOMMENDATIONS

A few things may be done to improve this study and further research on the processes of *B. anthracis* germination.

THE AFM CONTROL SHOULD BE EXPOSED TO TRIS-HCL, INCUBATED, AND RE-IMAGED TO REDUCE VARIABILITY BETWEEN SAMPLES.

A LARGER AFM SAMPLE OF L-ALANINE AND L-ALANINE+INOSINE SHOULD BE TAKEN. The most efficient way to obtain a large sample is to image dense populations of cells. Height data may not be obtainable using this method, but morphology comparison is accurate using only length and width data.

IMAGE SPORES WITH A HIGH RESOLUTION TIP IN REAL TIME TO SEE HOW EACH CONDITION AFFECTS THE NANO-SCALE RODLET STRUCTURE. This study must be done in liquid, just as Plomp studied his *Bacillus* spores in 2007. Detailed images for each condition could reveal differences in mechanisms for each germinant.

WORKS CITED

Chada, V. G., Sanstad, E. A., Wang, R., & Driks, A. (2003). Morphogenesis of Bacillus Spore Surfaces. *Journal of Bacteriology , 185* (21), 6255-6261.

Ferencko, L., Cote, M. A., & Rotmana, B. (2004). Esterase activity as a novel parameter of spore germination in Bacillus anthracis. *Biochemical and Biophysical Research Communications , 319*, 854-858.

Gould, G. (1977). Recent Advances in the Understanding of Resistance and Dormancy in Bacterial Spores. *J Appl Bacteriol , 42*, 297-309.

Iijima, N., Tanimoto, N., Emoto, Y., Morita, Y., Uematsu, K., Murakami, T., et al. (2003). Purification and characterization of three isoforms of chrysophsin, a novel antimicrobial peptide in the gills of the red sea bream, Chrysophrys major. *Eur. J. Biochem* (270), 675-686.

Jagtap, P., Michailidis, G., Zielke, R., Walker, A. K., Patel, N., Strahler, J. R., et al. (2006). Early events of <I>Bacillus anthracis</I> germination identified by time-course quantitative proteomics. *Proteomics , 6* (19), 5199-5211.

Moir, A. (2006). How do spores germinate? *Journal of Applied Microbiology* , 526-530.

Moir, A., & Smith, D. A. (1990). The Genetics of Bacterial Spore Germination. *Annu. Rev. Microbiol. , 44*, 531-53.

Paidhungat, M., & Setlow, P. (1999). Isolation and Characterization of Mutations in Bacillus subtilis That Allow Spore Germination in the Novel Germinant d-L-Alanine. *J Bacteriol , 181* (11), 3341-3350.

Plomp, M., Leighton, T. J., Wheeler, K. E., & Malkin, A. J. (2005). The High-Resolution Architecture and Structural Dynamics of Bacillus Spores. *Biophysical Journal , 88*, 603-608.

Plomp, M., Leighton, T. J., Wheeler, K. E., Hill, H. D., & Malkin, A. J. (2007). In vitro high-resolution structural dynamics of single germinating bacterial spores. *PNAS , 104* (23), 9644-9649.

Plomp, M., Leighton, T. J., Wheeler, K. E., Pitesky, M. E., & Malkin, A. J. (2005). Bacillus atrophaeus Outer Spore Coat Assembly and Ultrastructure. *Langmuir , 21*, 10710-10716.

Todar, K. (2004, June 4). The Good, the Bad, and the Deadly. *SCIENCE Magazine , 304*, p. 1421.

Wang, R., Krishnamurthy, S. N., Jeong, J.-S., Driks, A., Mehta, M., & Gingras, B. A. (2007). Fingerprinting Species and Strains of Bacilli Spores by Distinctive Coat Surface Morphology. *Langmuir , 23* (20), 10230-10234.

Zaman, M. S., Goyal, A., Dubey, G. P., Gupta, P. K., Chandra, H., Das, T. K., et al. (2005). Imaging and Analysis of Bacillus anthracis Spore Germination. *Microscopy Research and Technique , 66*, 307-311.

APPENDIX A – CONTROL AFM IMAGES

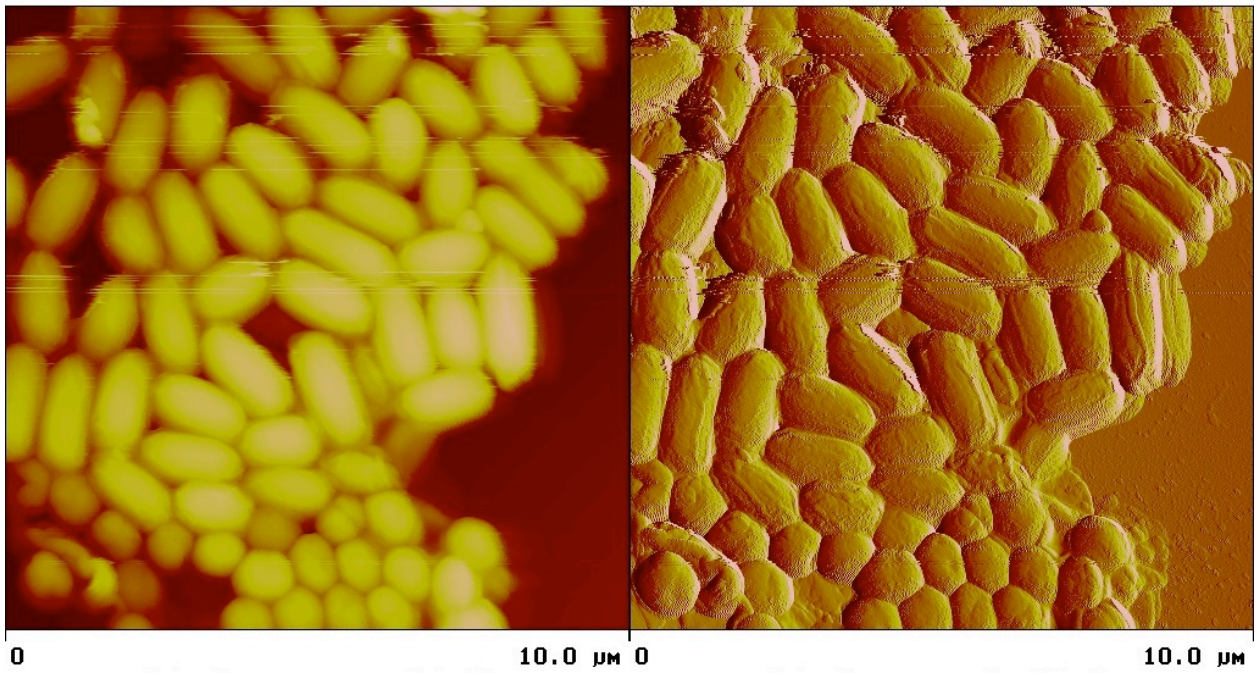

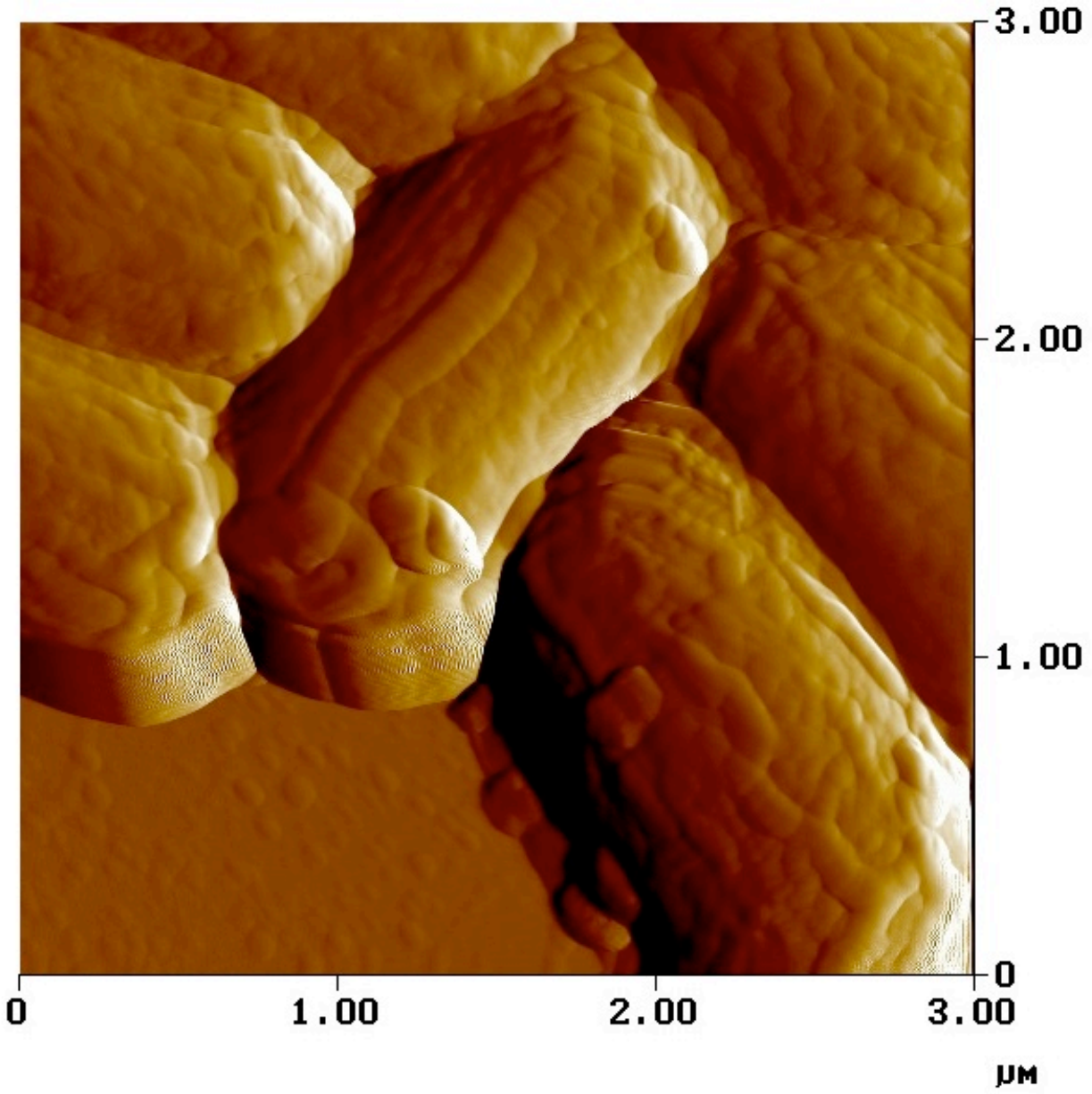
3.00
2.00
1.00
0
0
1.00
2.00
3.00
µm

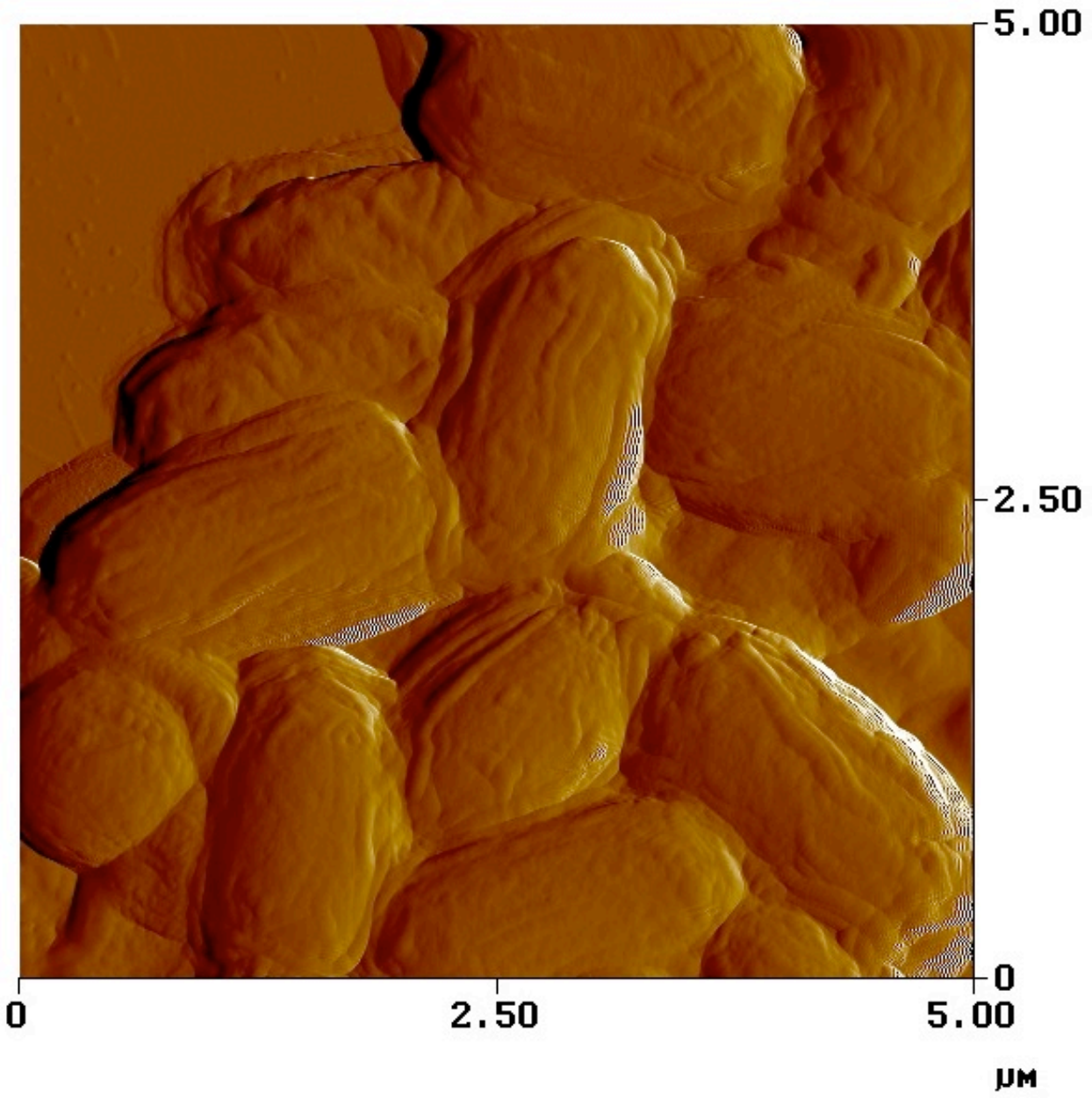
5.00
2.50
0
0
2.50
5.00
µm

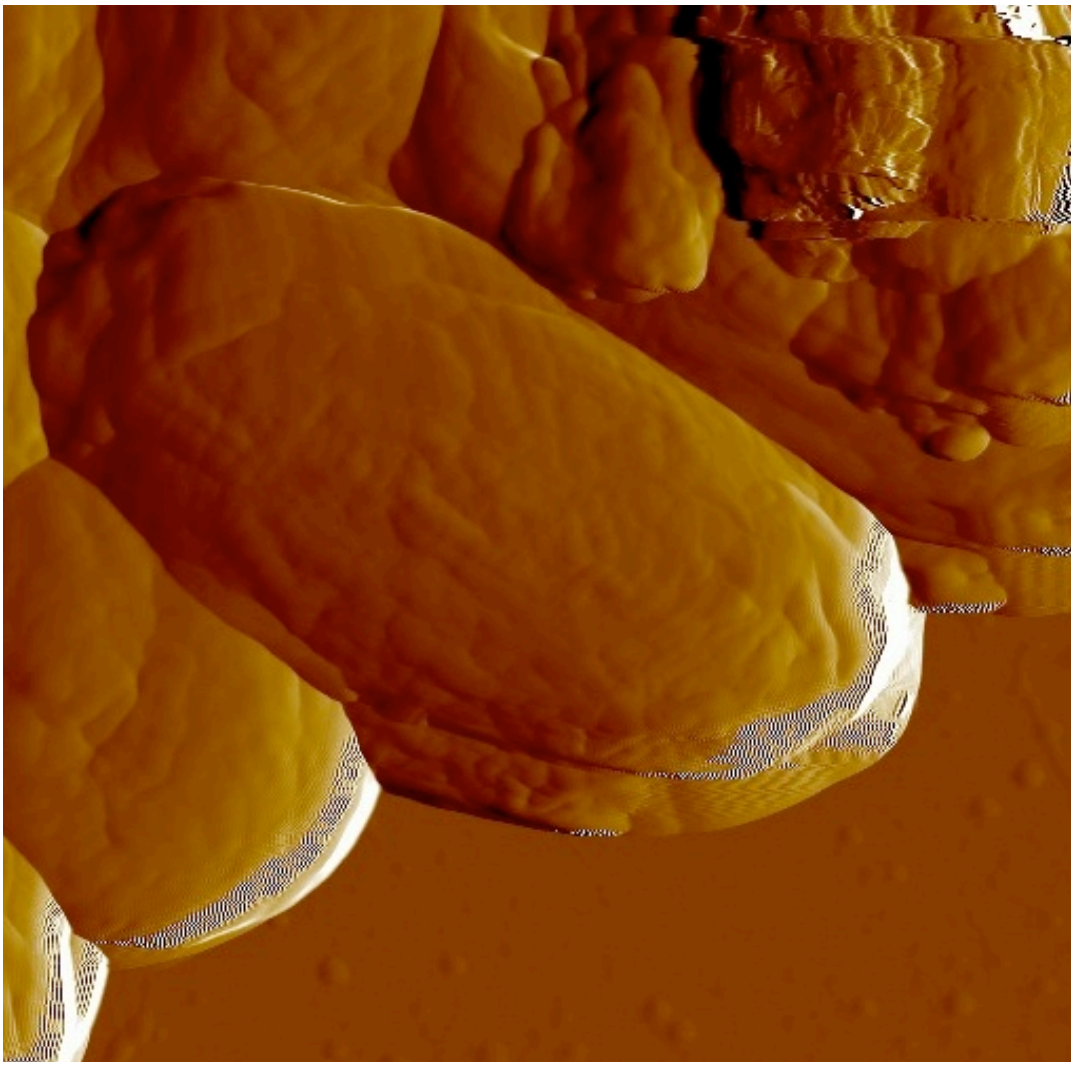

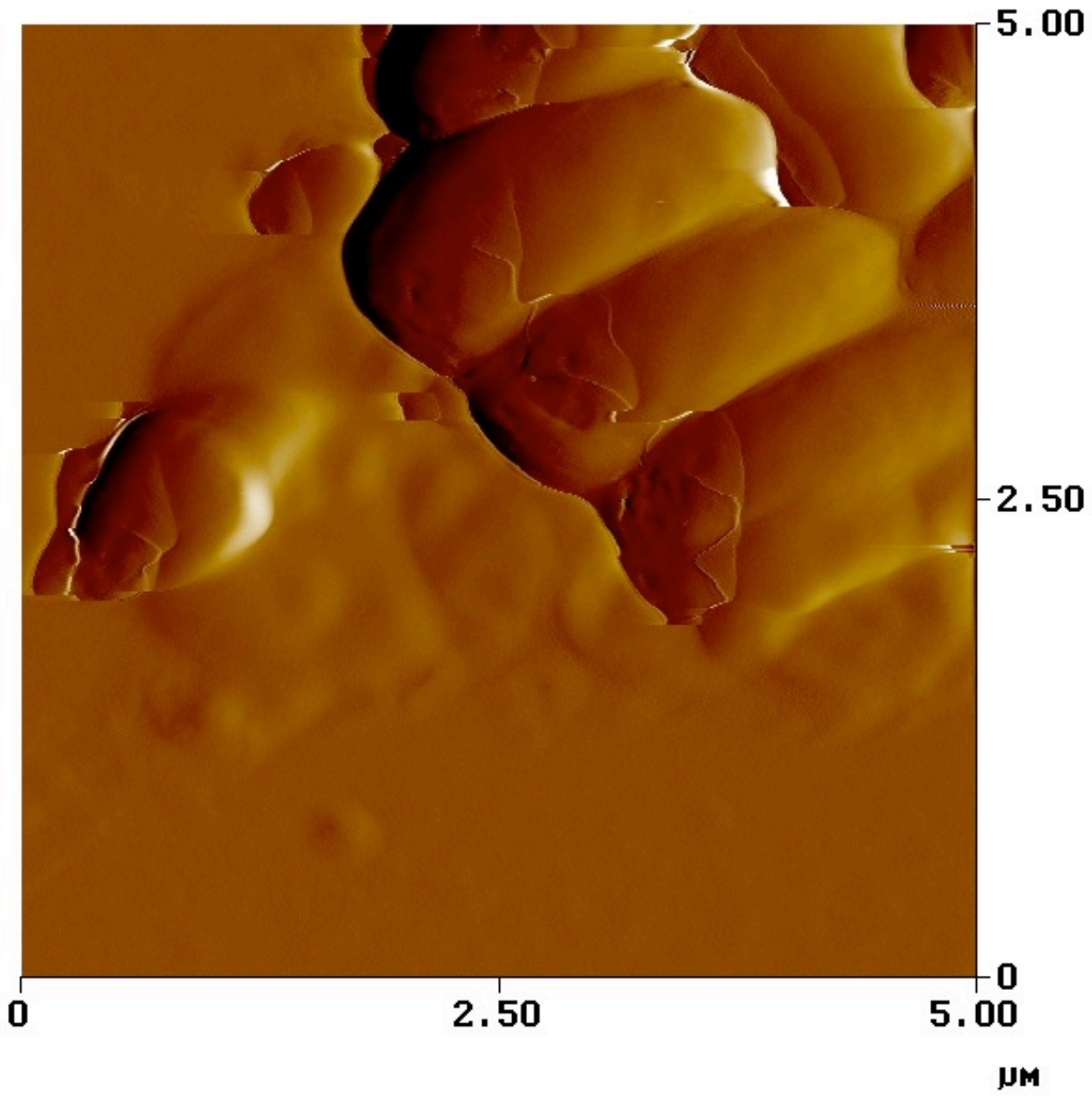
5.00
2.50
0
0
2.50
5.00
µm

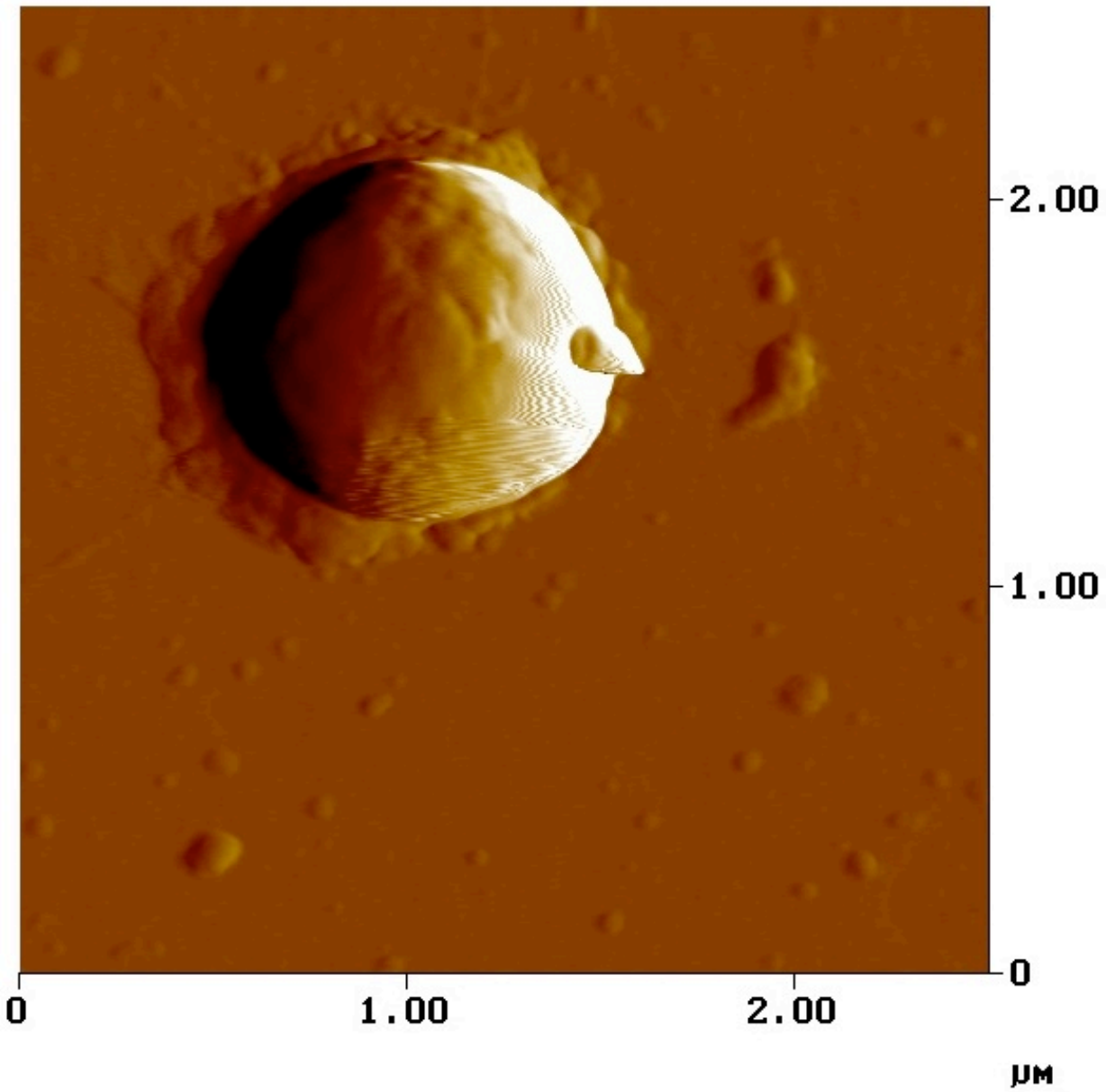
2.00
1.00
0
0
1.00
2.00
µm

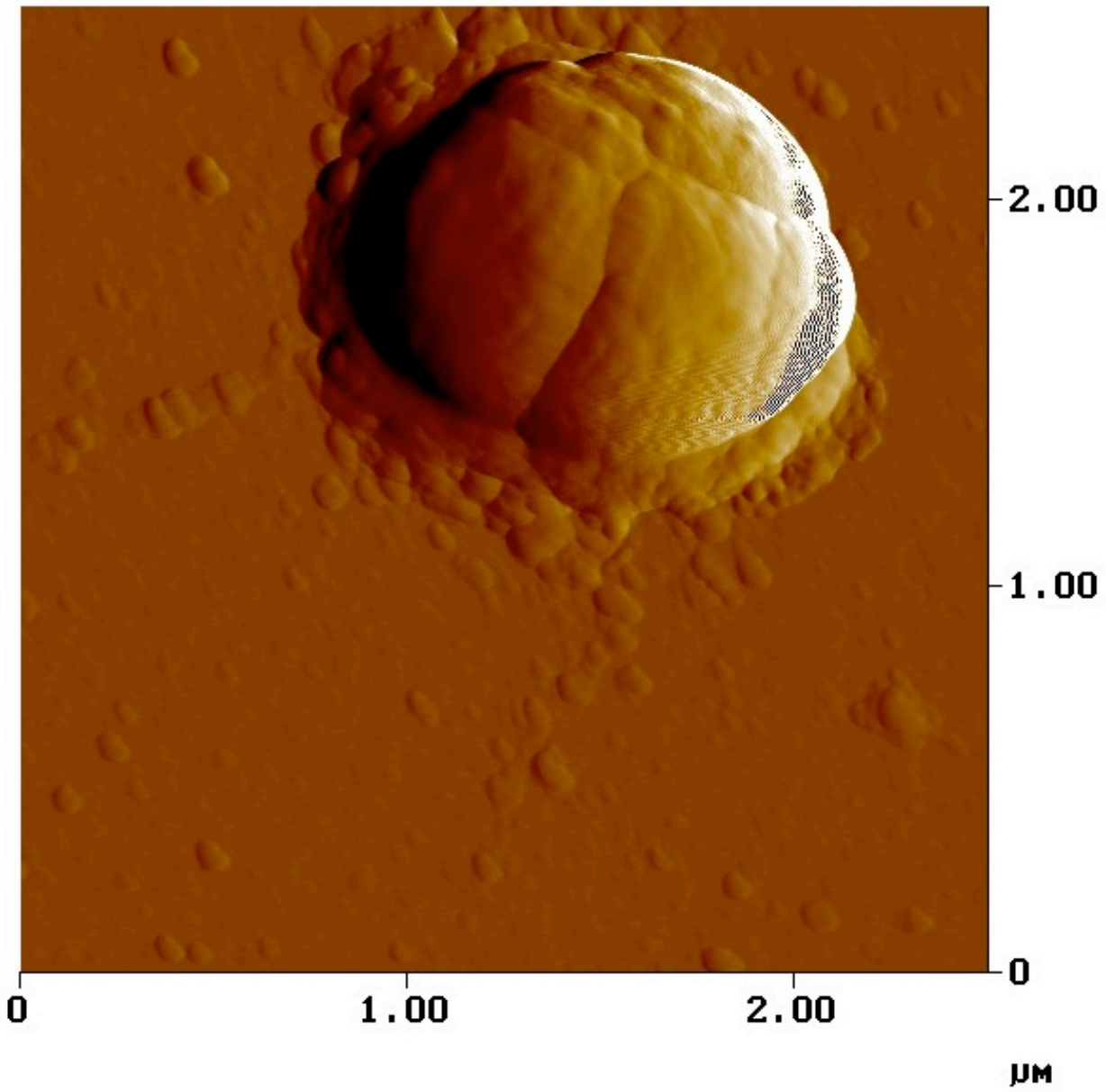
2.00
1.00
0
0
1.00
2.00
µm

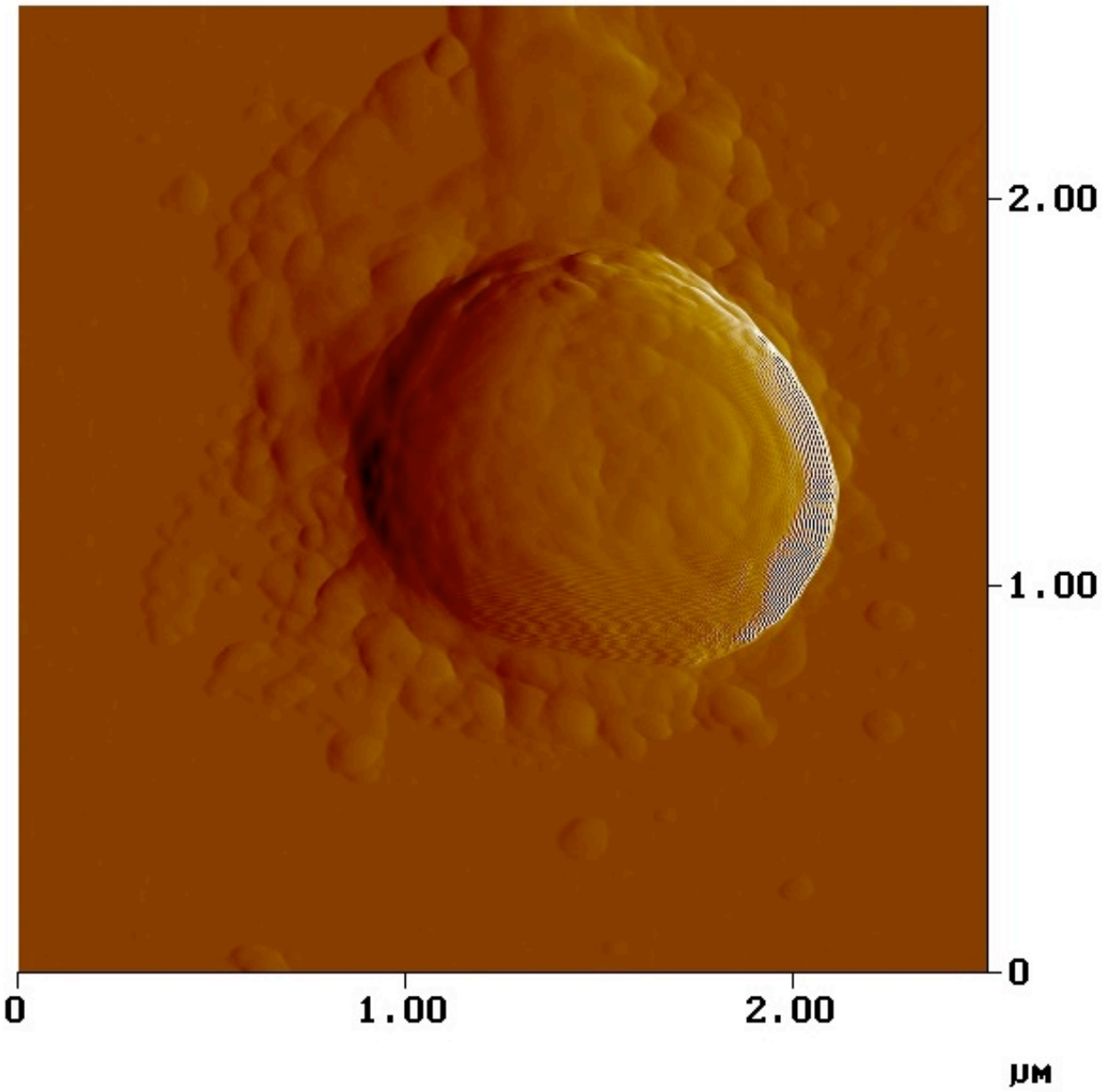
2.00
1.00
0
0
1.00
2.00
µm

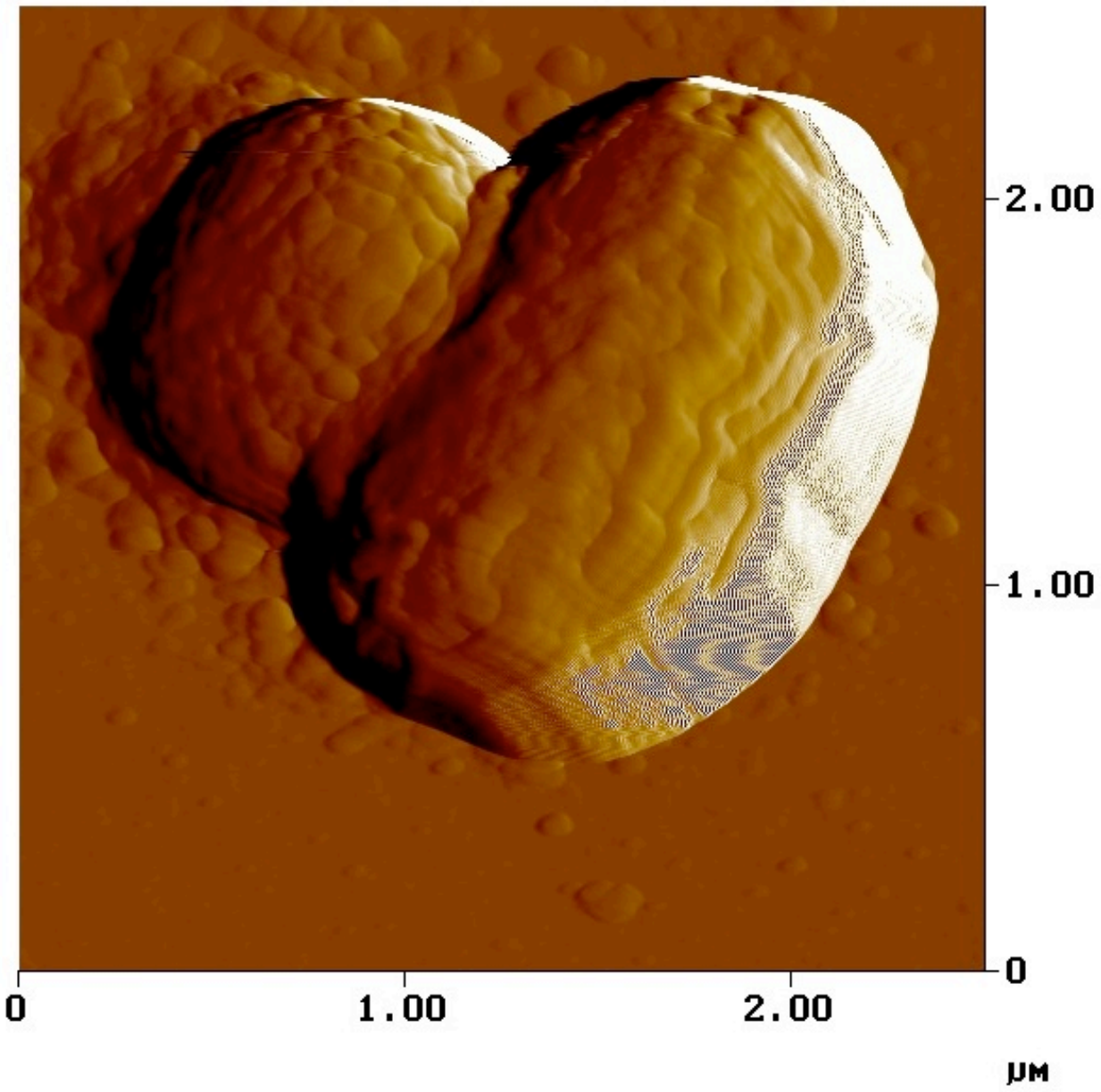
2.00
1.00
0
0
1.00
2.00
µm

APPENDIX B – INOSINE AFM IMAGES

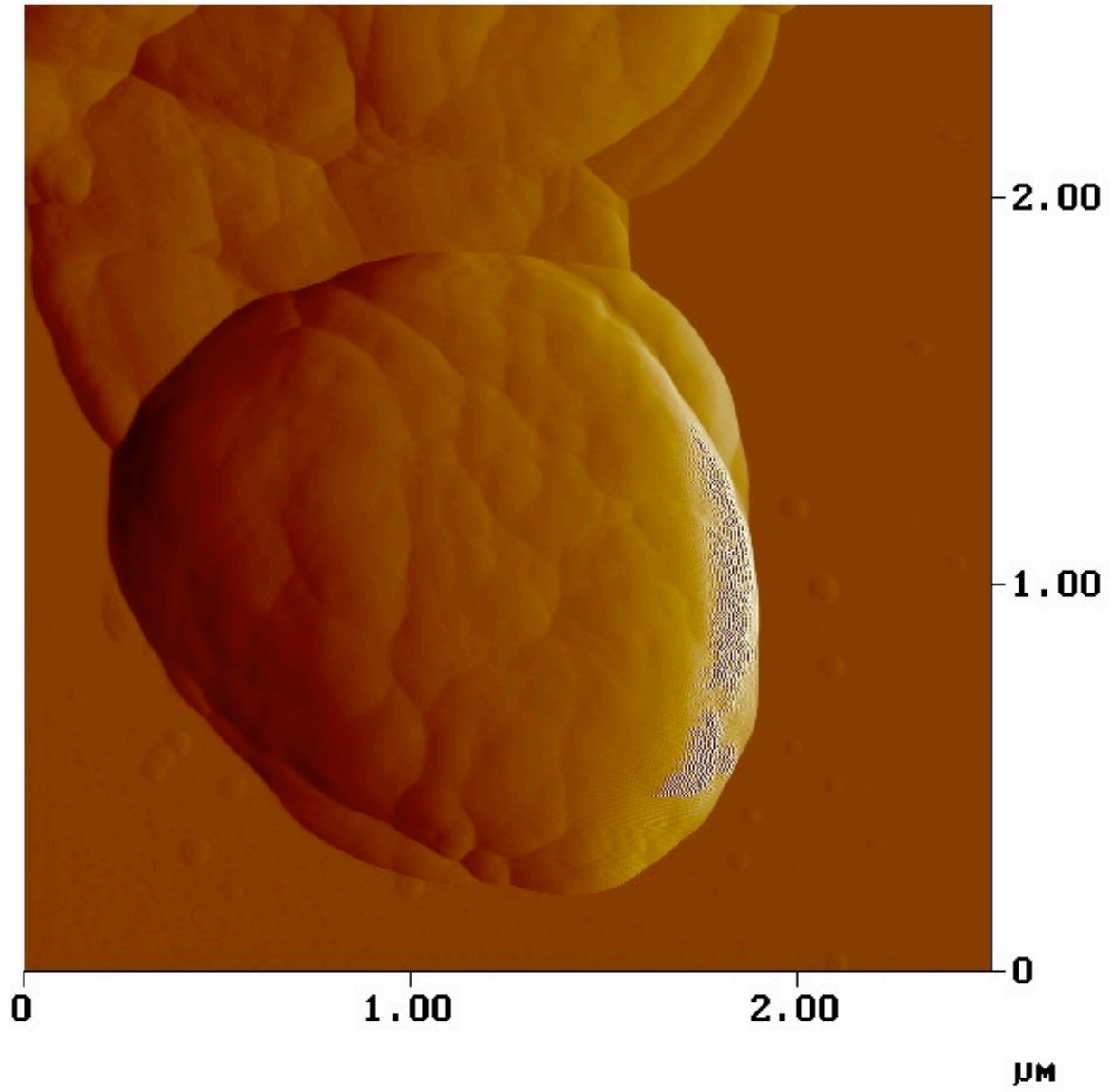

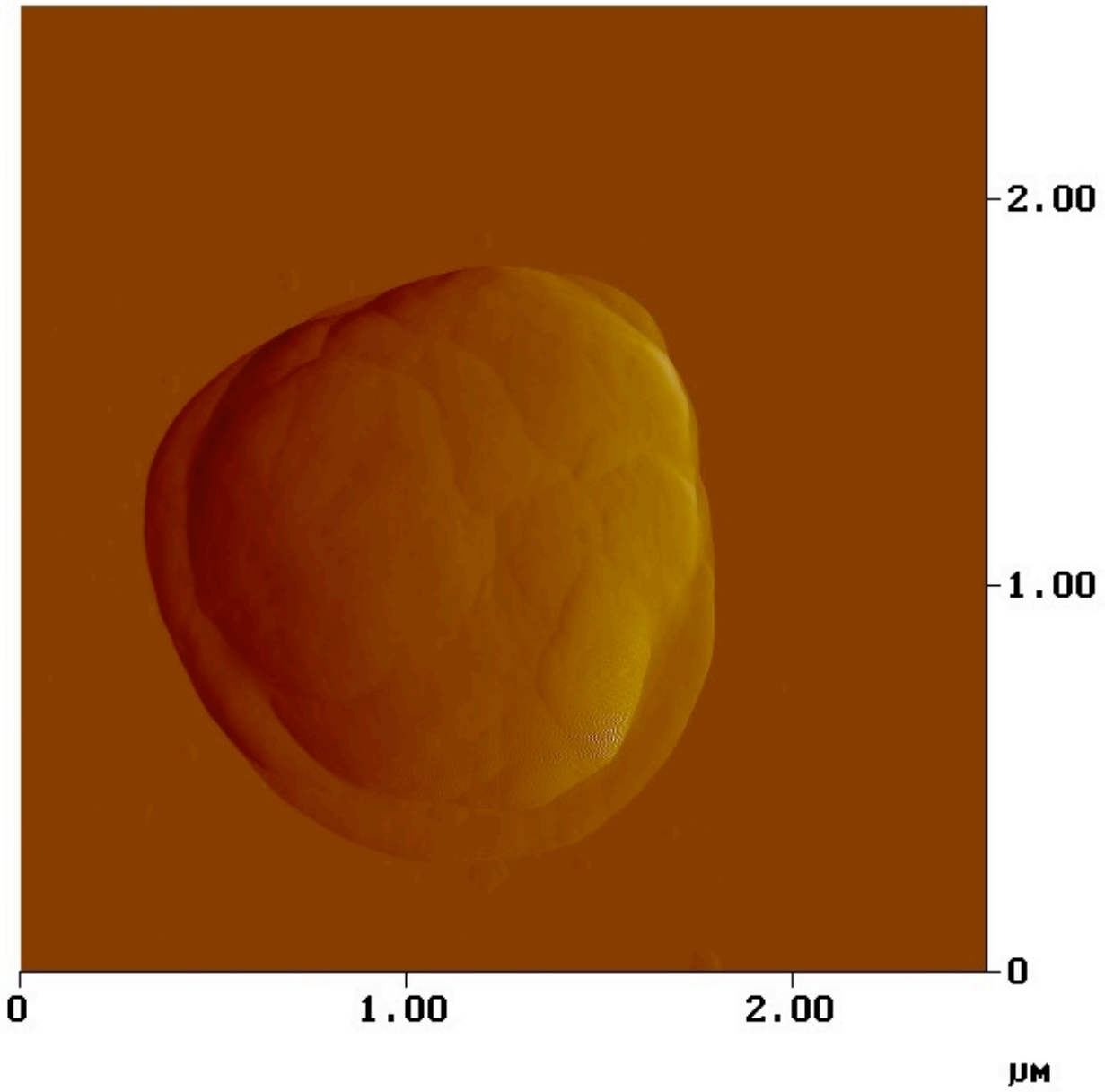
2.00
1.00
0
0
1.00
2.00
µm

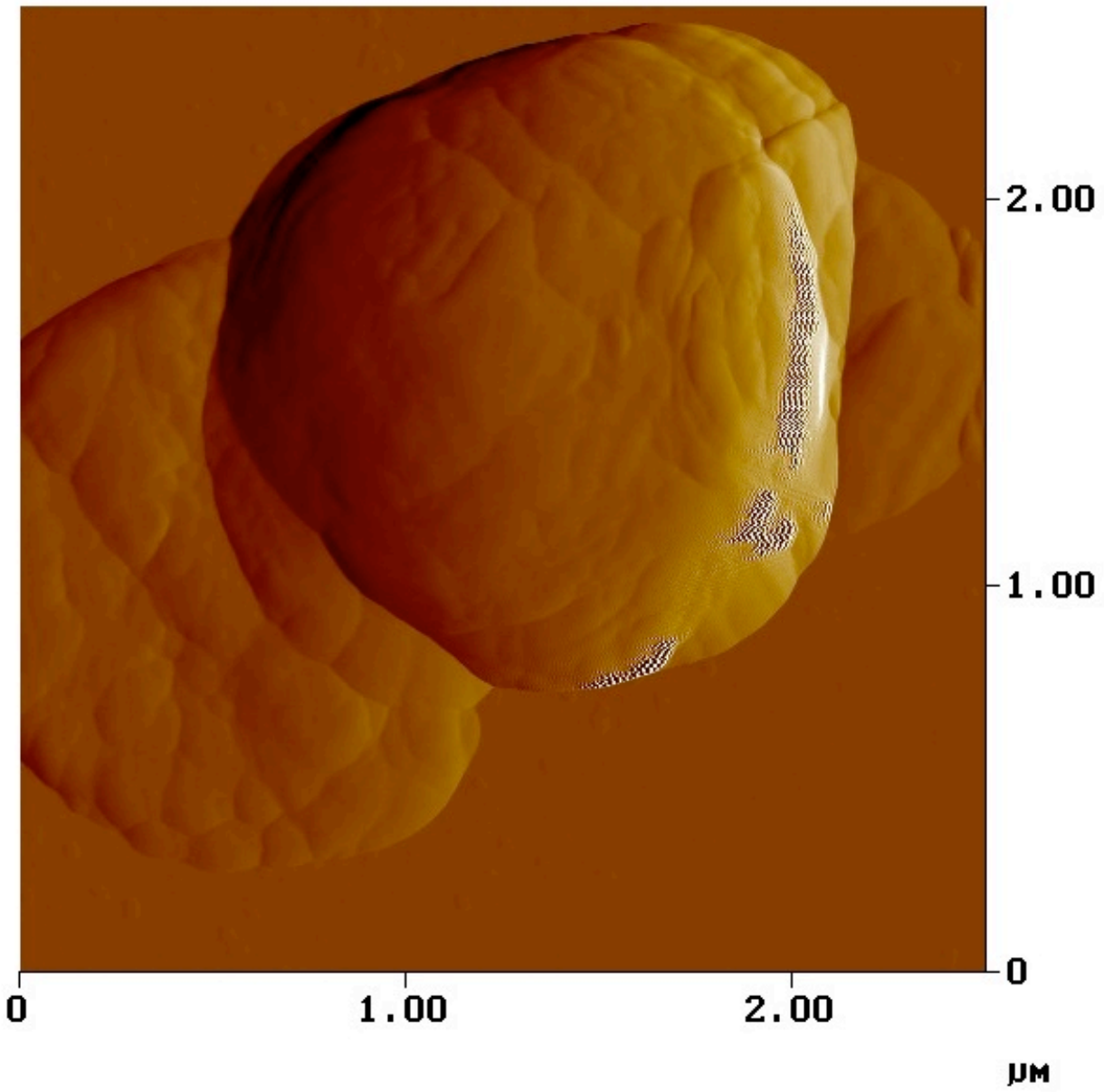
2.00
1.00
0
0
1.00
2.00
µm

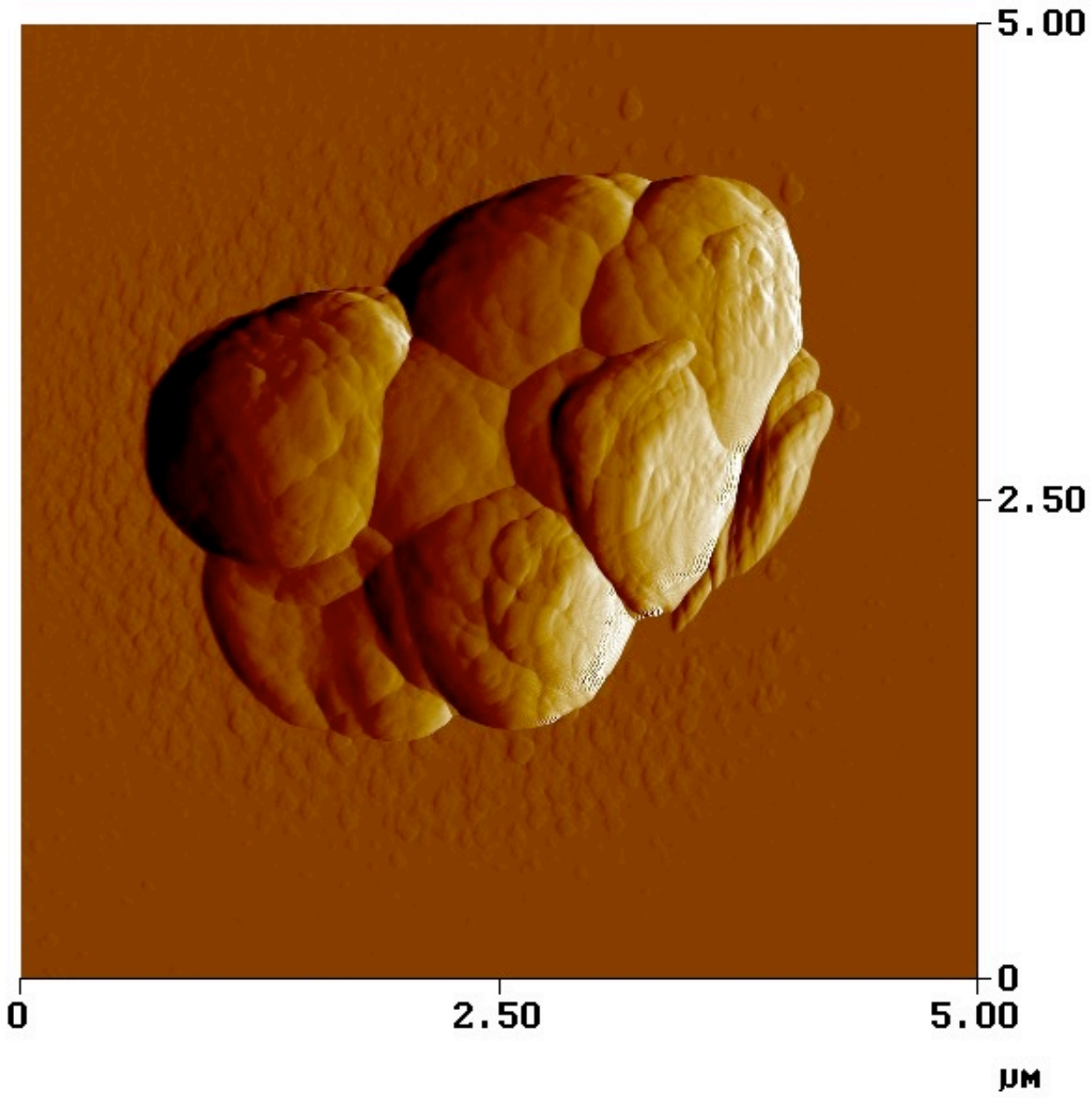
5.00
2.50
0
0
2.50
5.00
µm

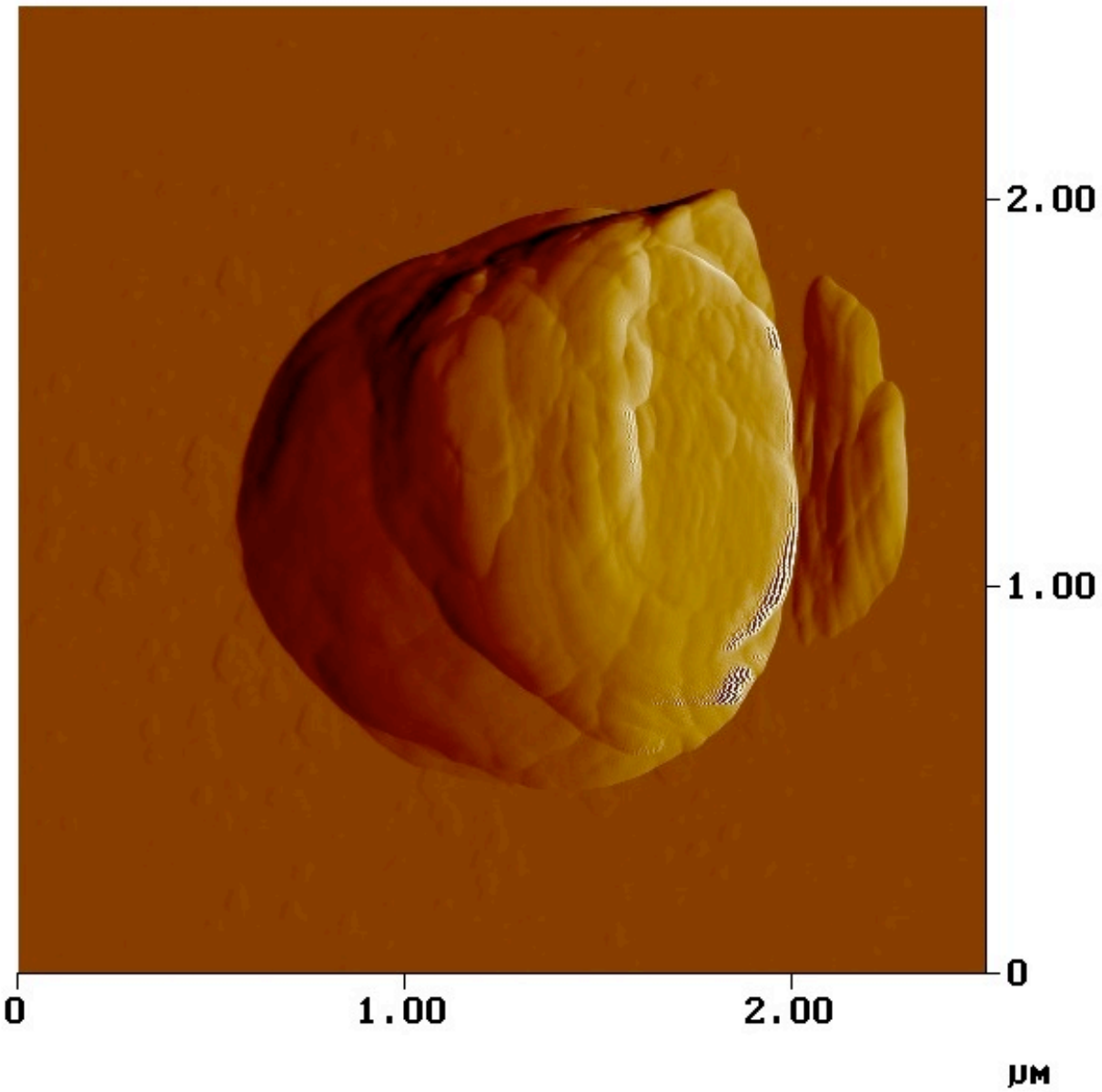
2.00
1.00
0
0
1.00
2.00
µm

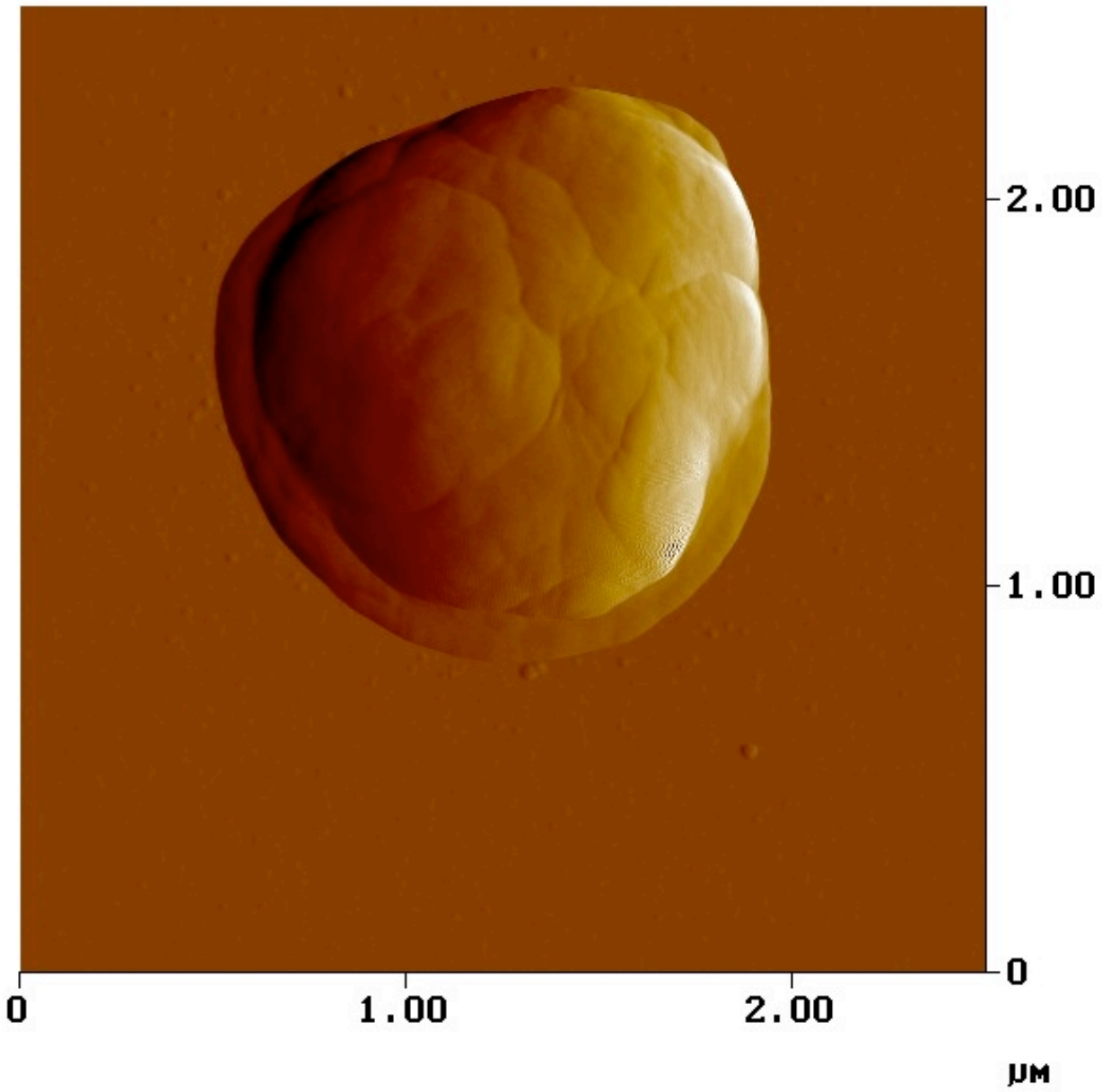
2.00
1.00
0
0
1.00
2.00
µm

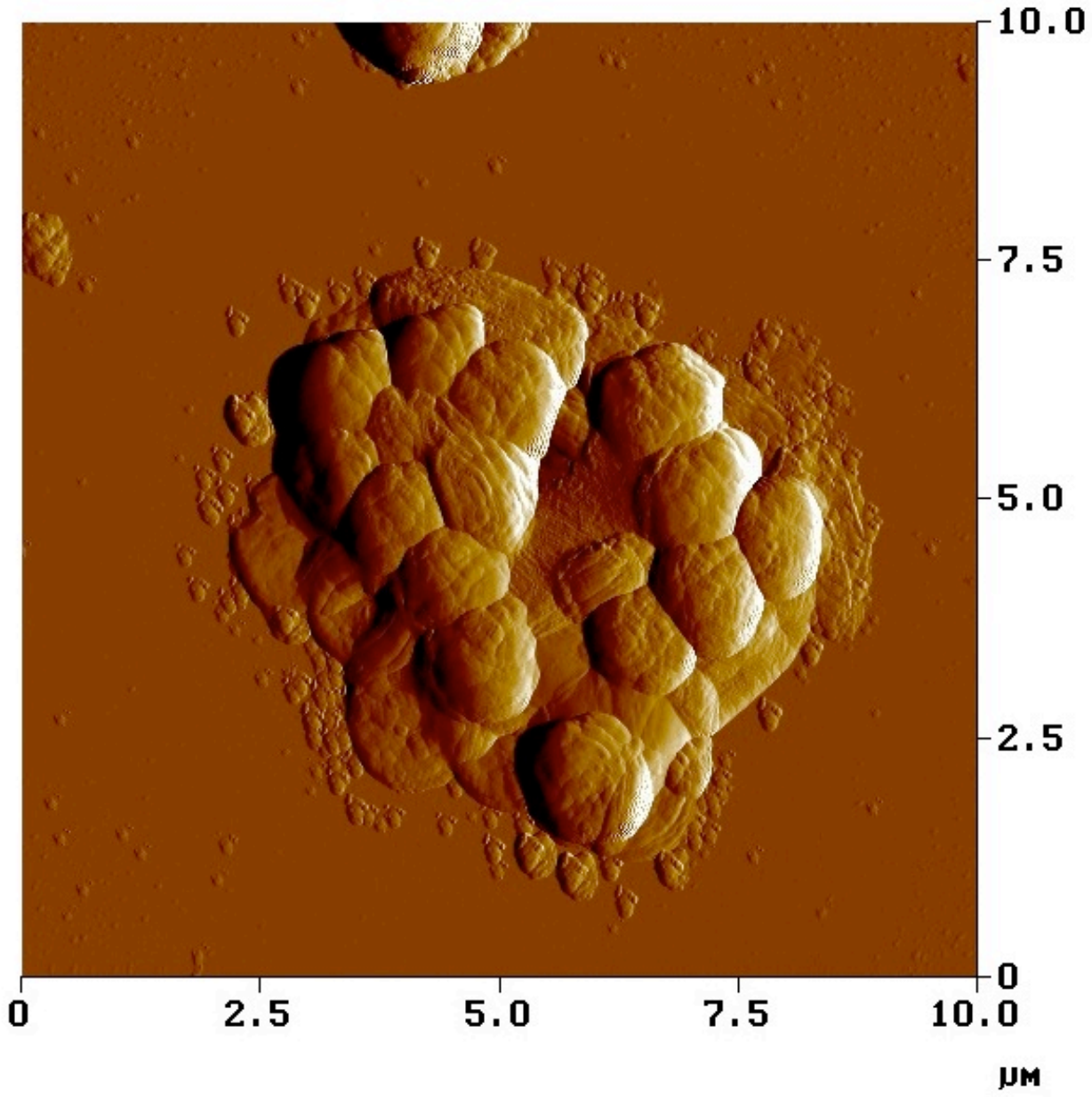
10.0
7.5
5.0
2.5
0
0
2.5
5.0
7.5
10.0
µm

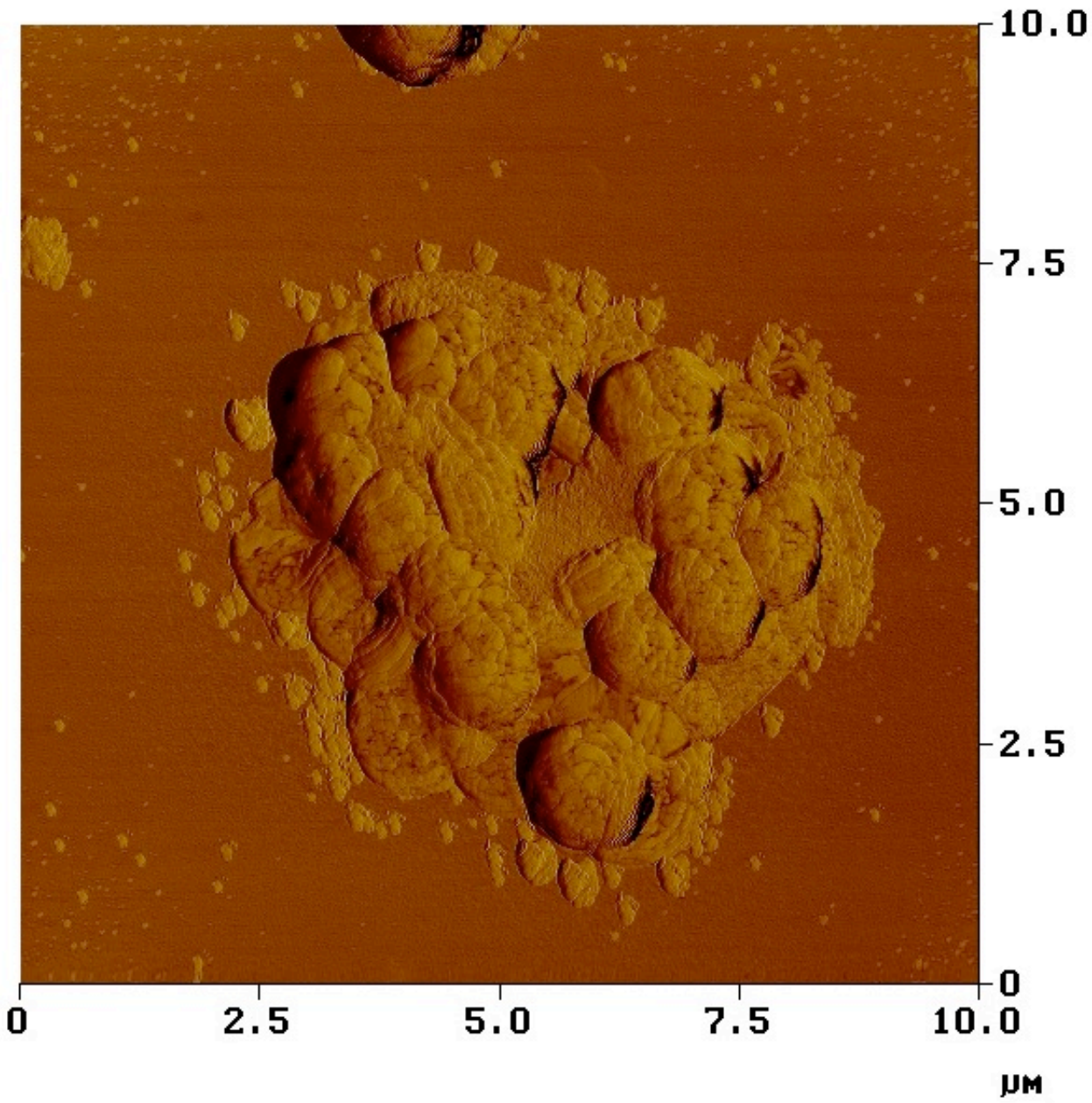

Phase Image

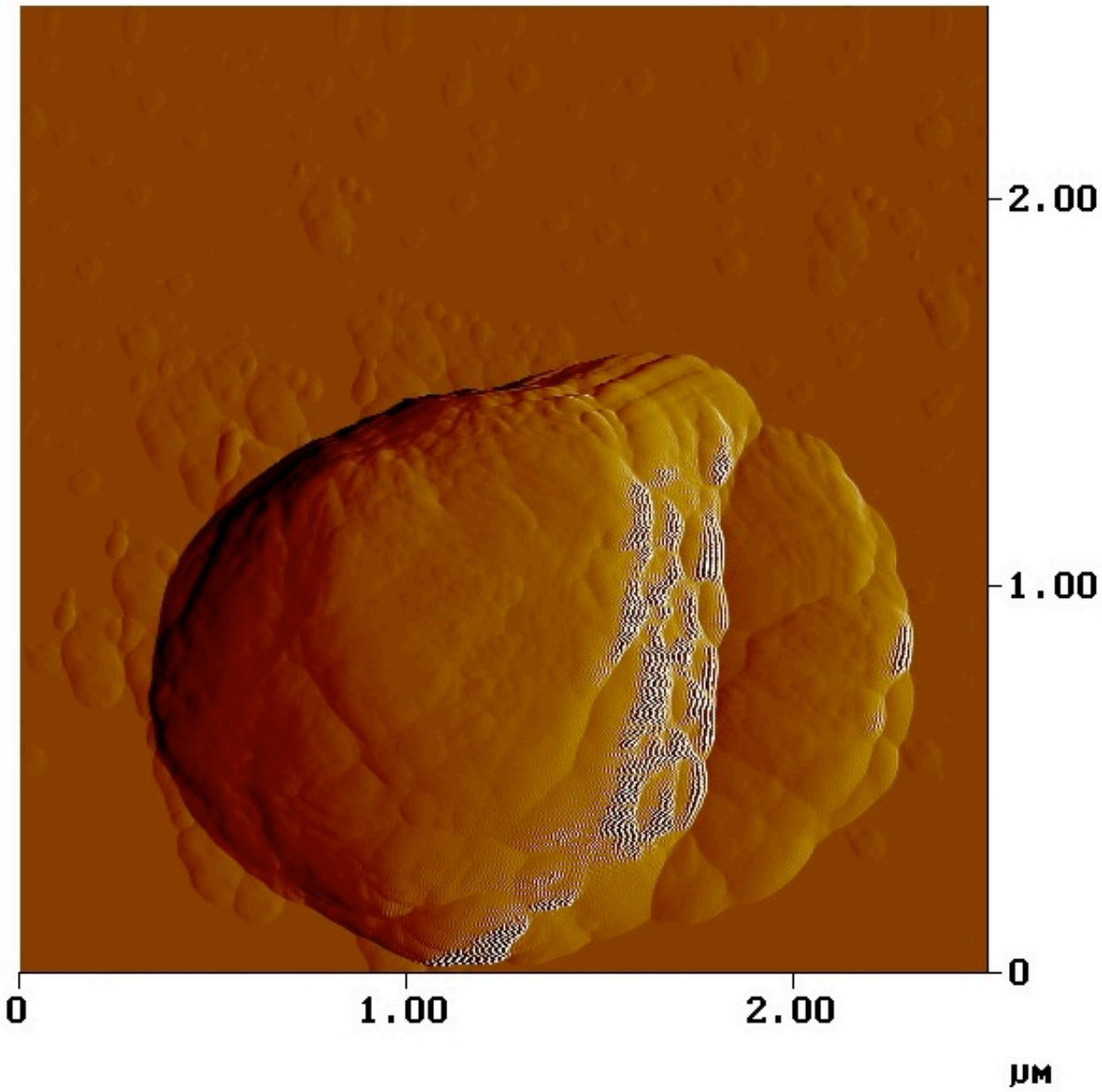
2.00
1.00
0
0
1.00
2.00
µm

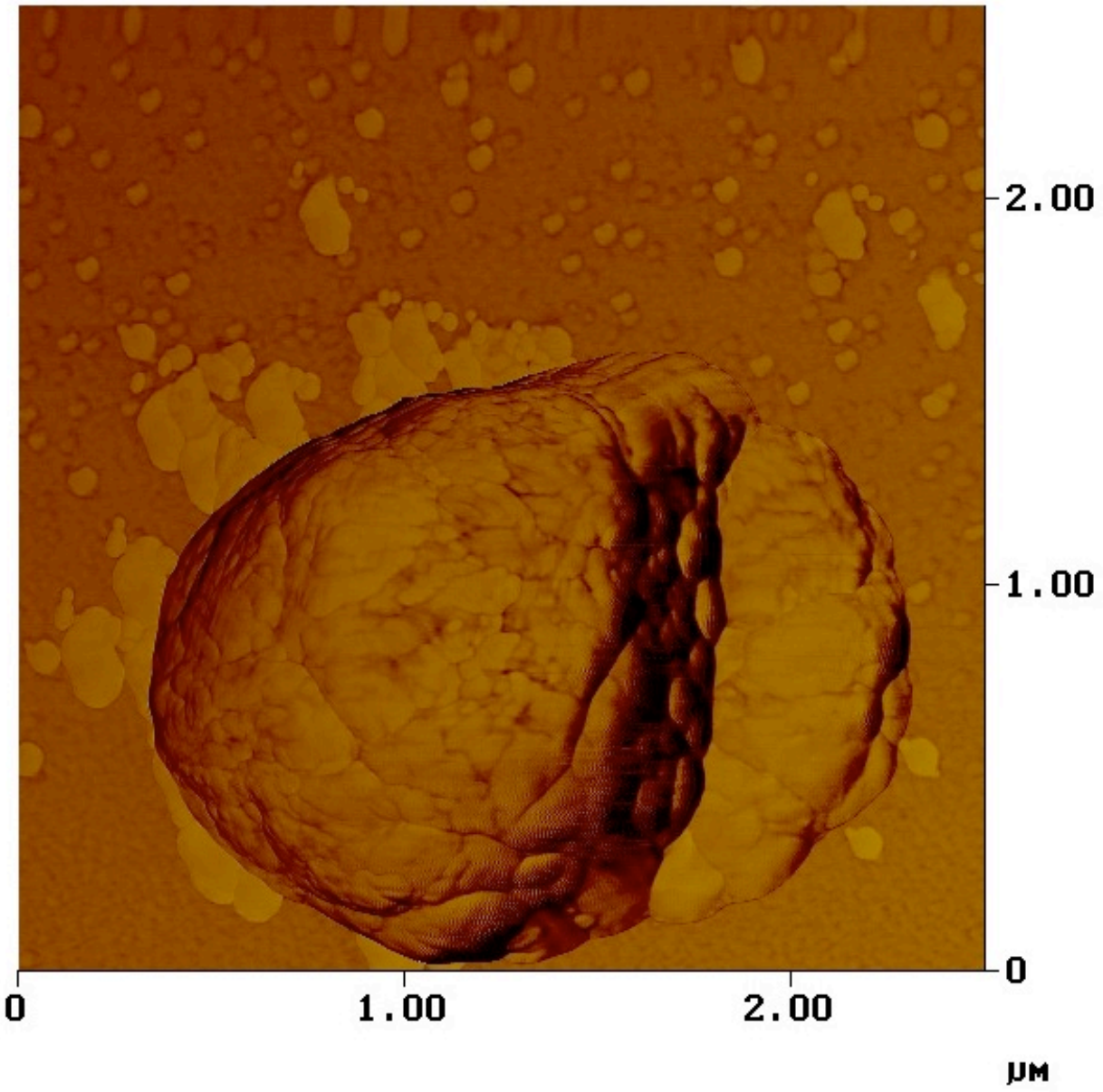

Phase Image

APPENDIX C – L-ALANINE AFM IMAGES

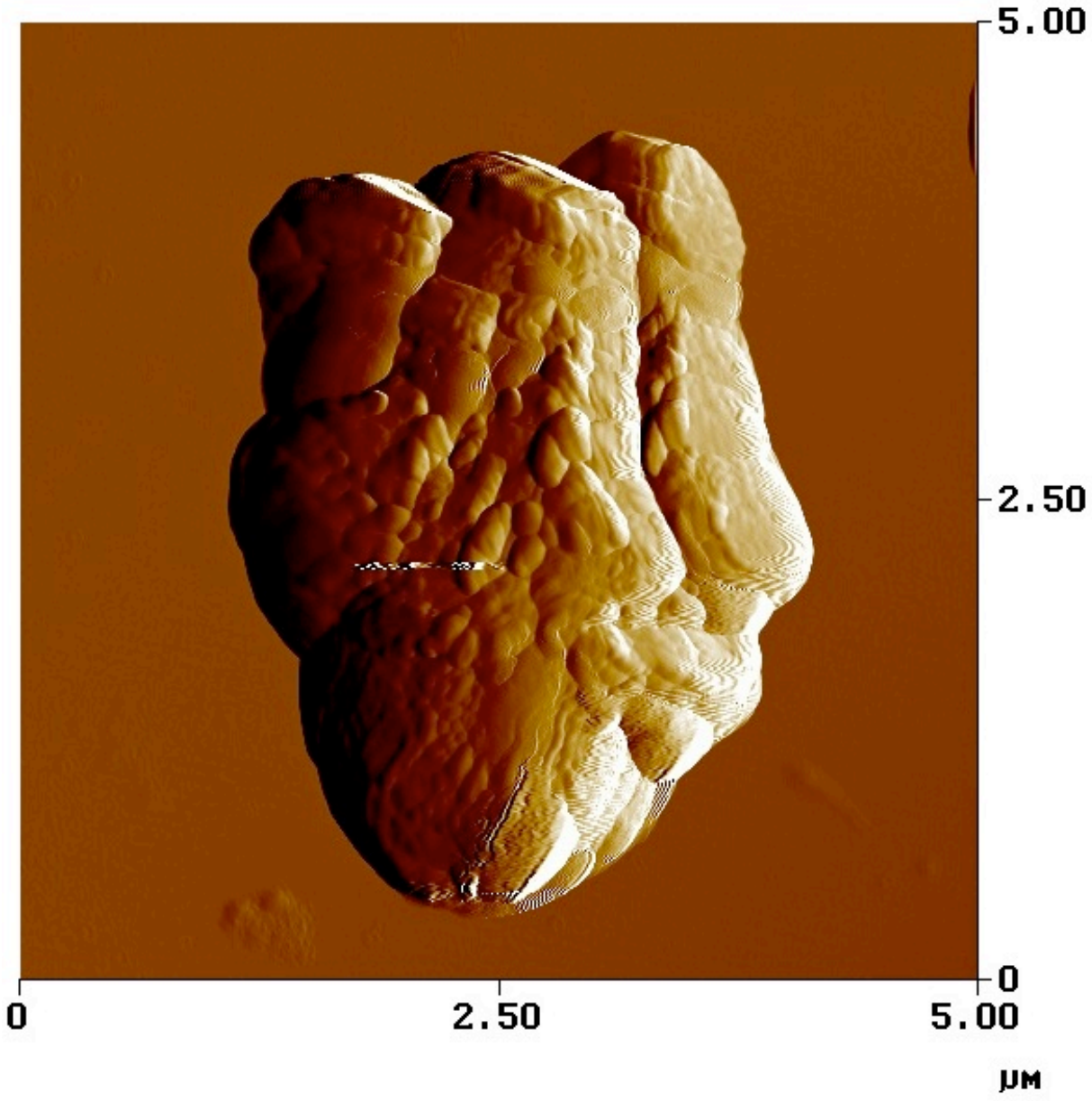

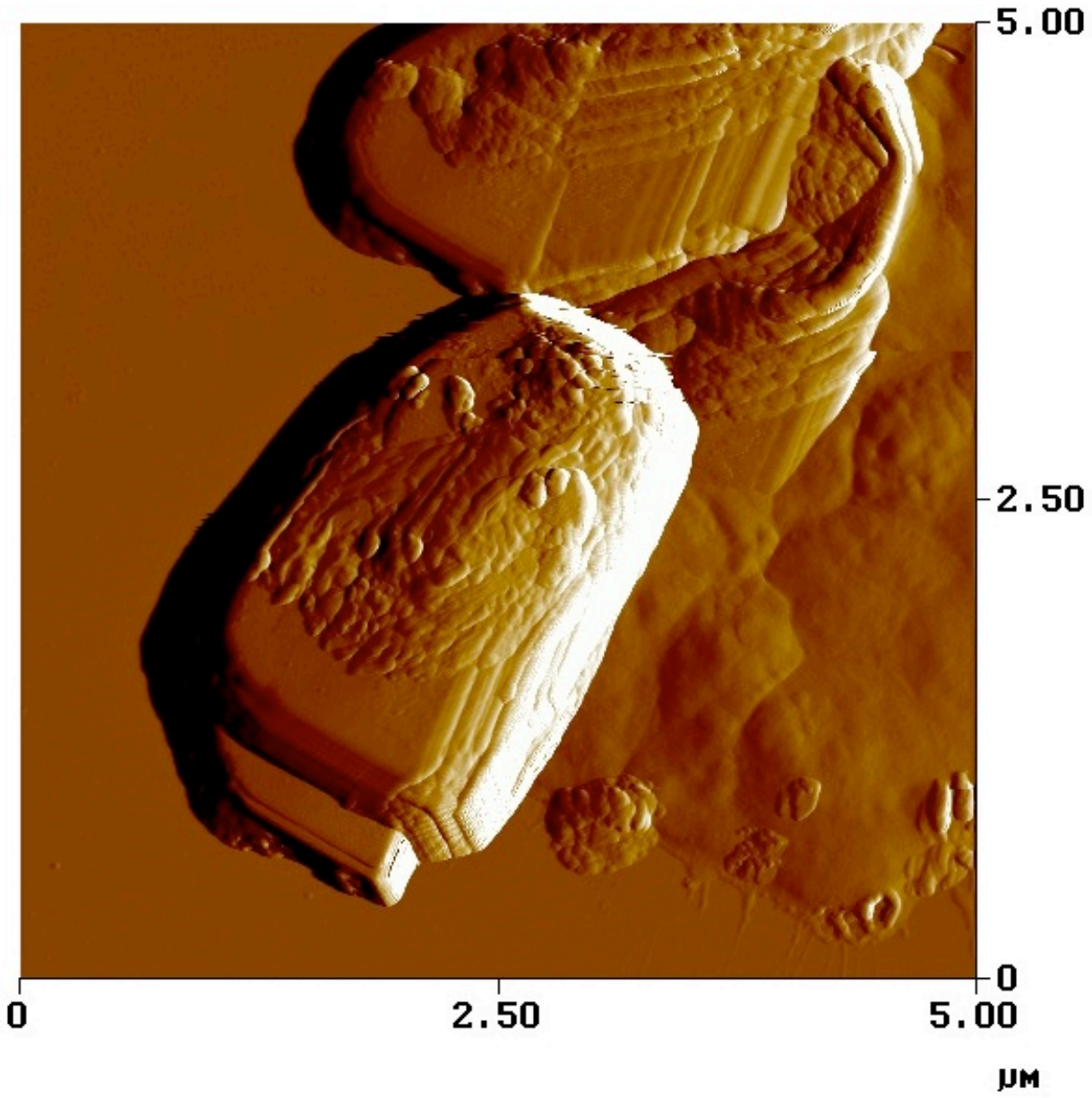
5.00
2.50
0
0
2.50
5.00
µm

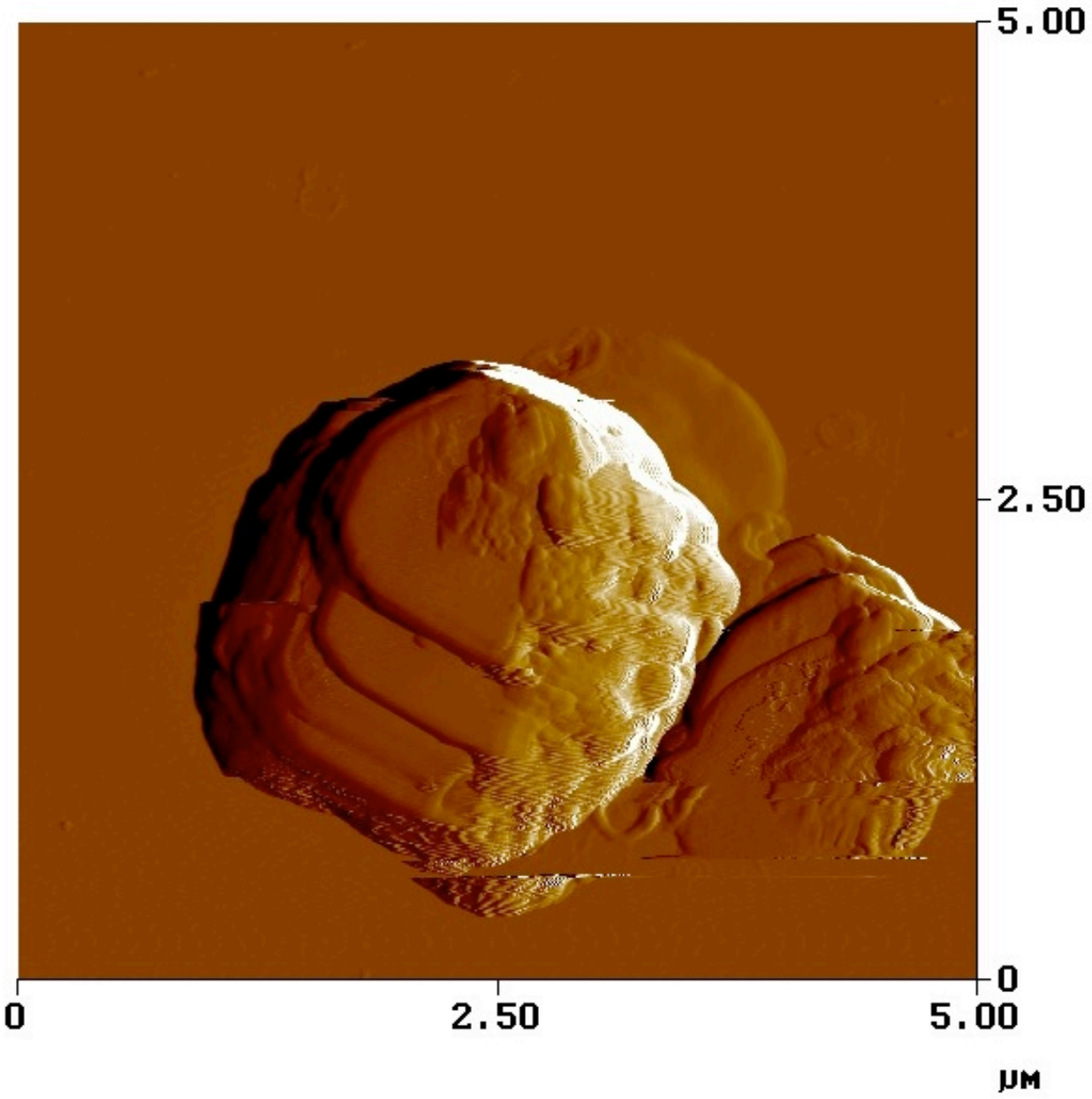
5.00
2.50
0
0
2.50
5.00
µm

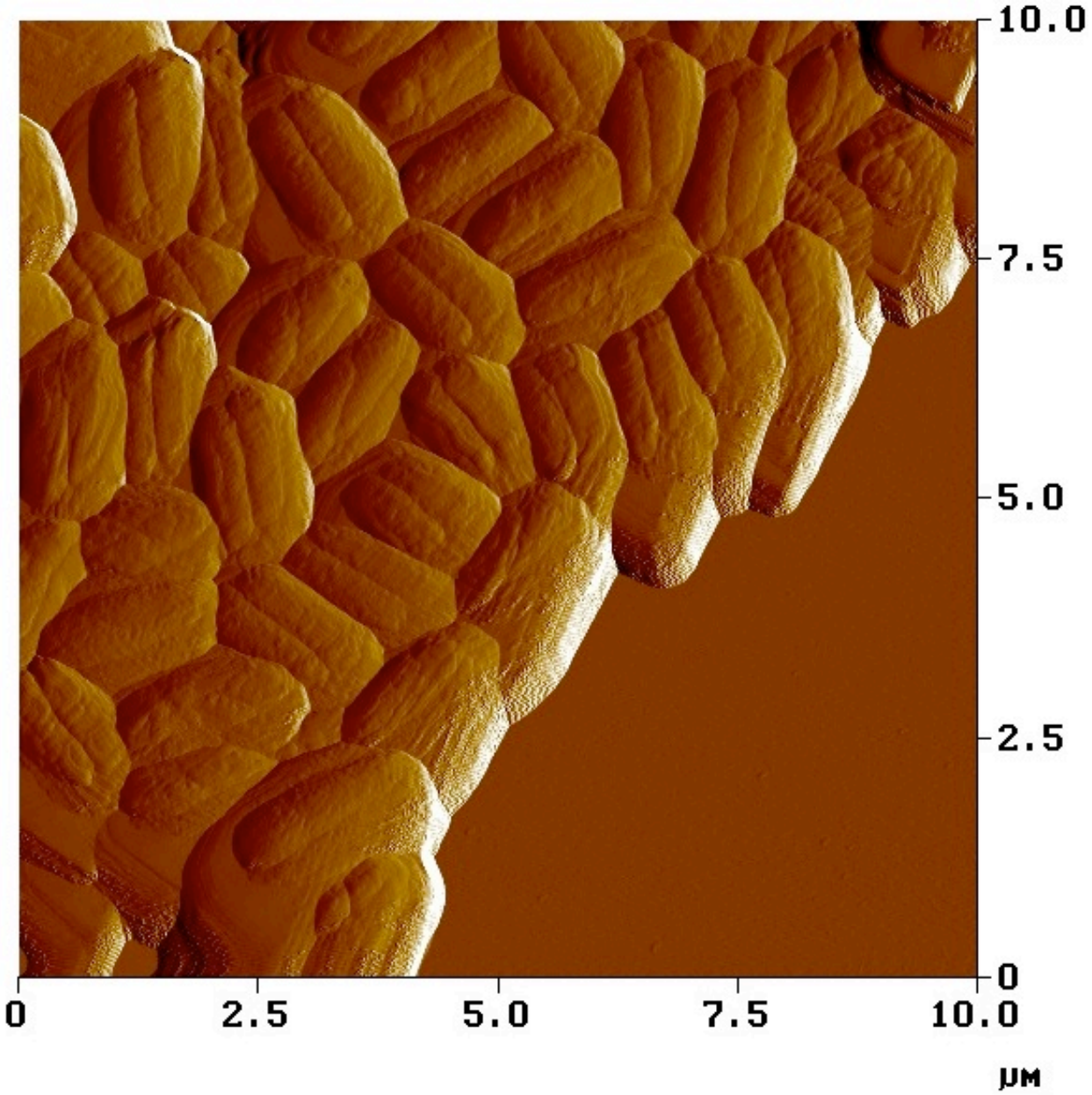
10.0
7.5
5.0
2.5
0
0
2.5
5.0
7.5
10.0
µm

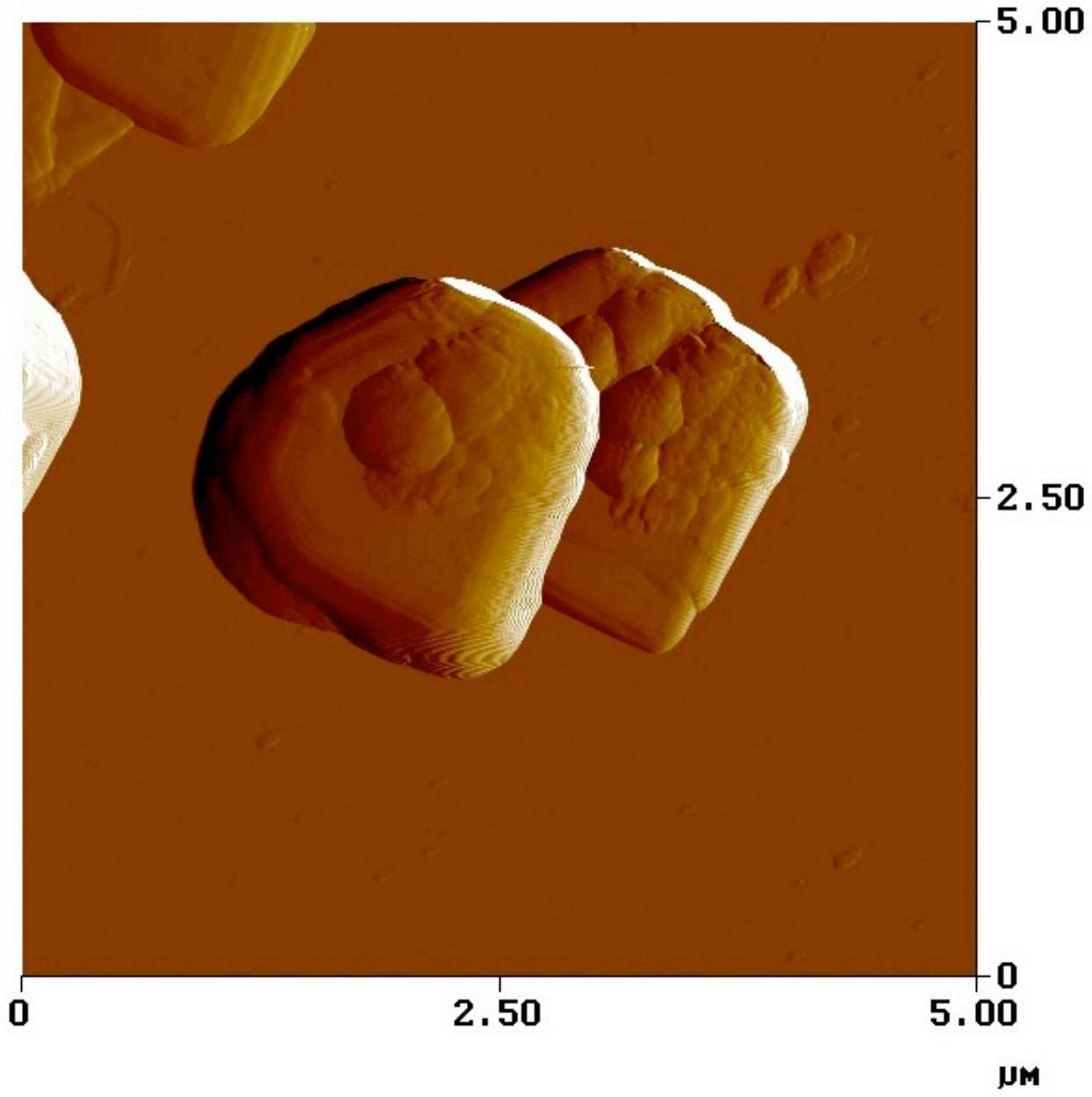
5.00
2.50
0
0
2.50
5.00
µm

APPENDIX D – L-ALANINE+INOSINE AFM IMAGES

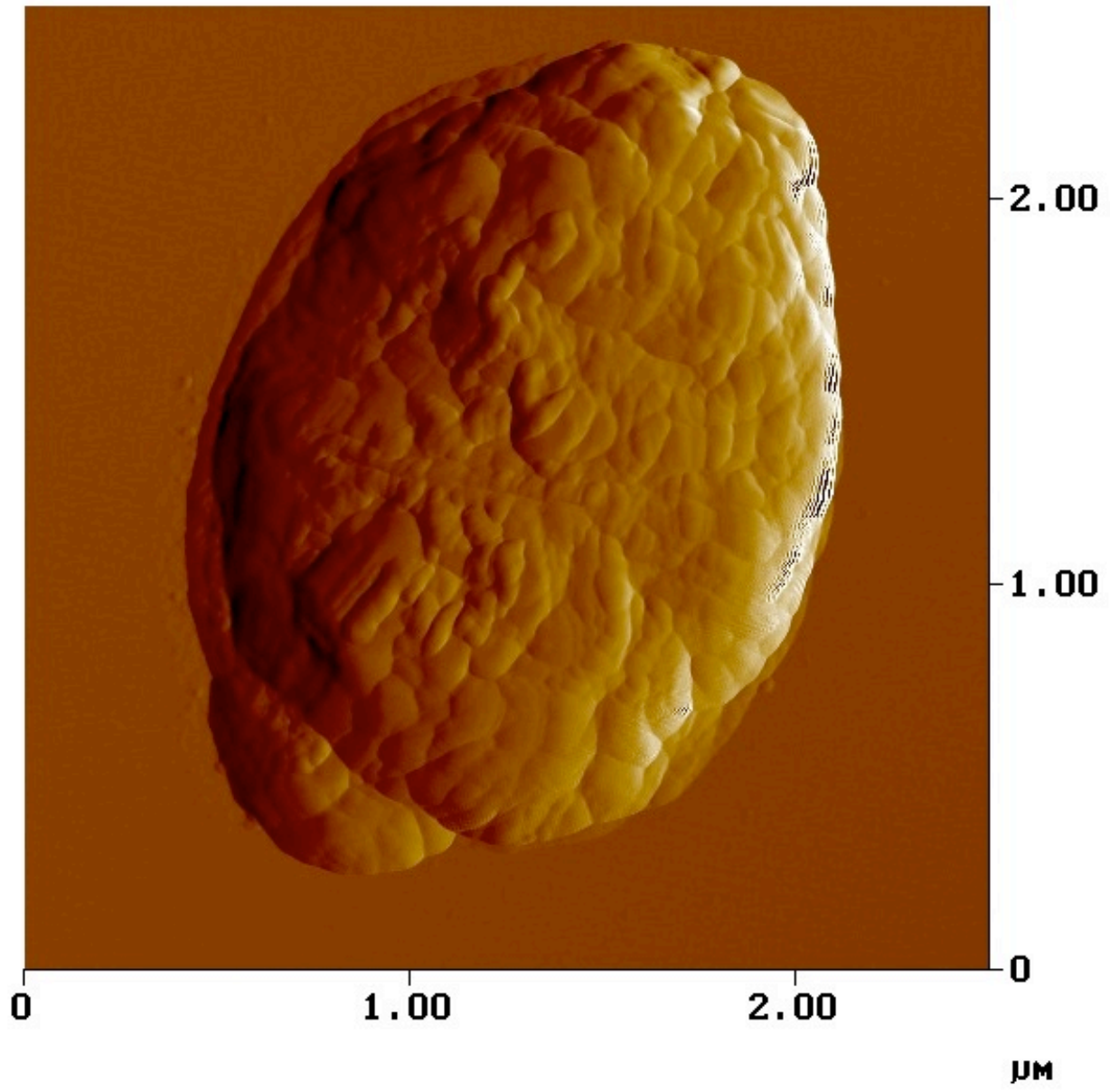

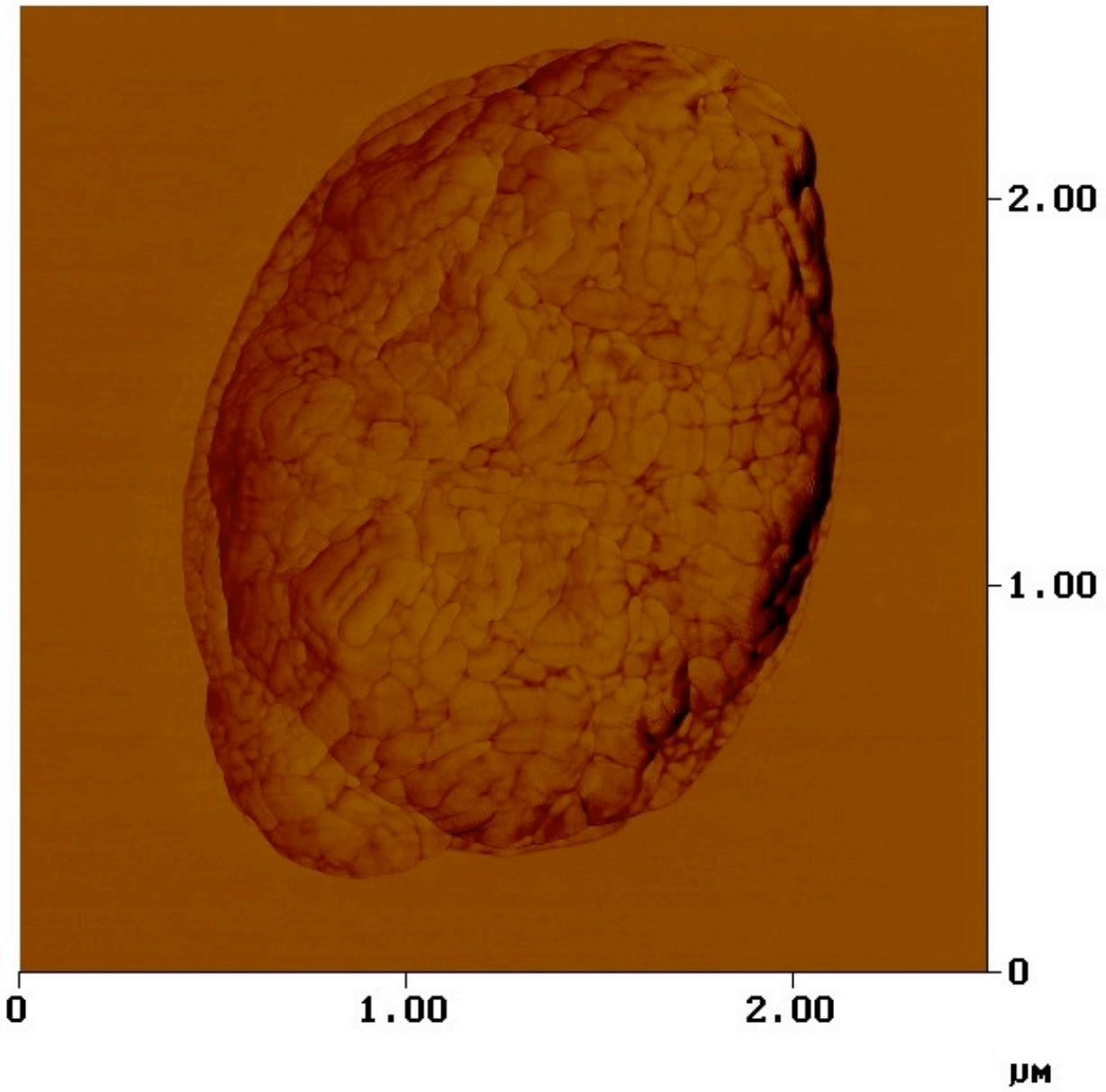

Phase Image

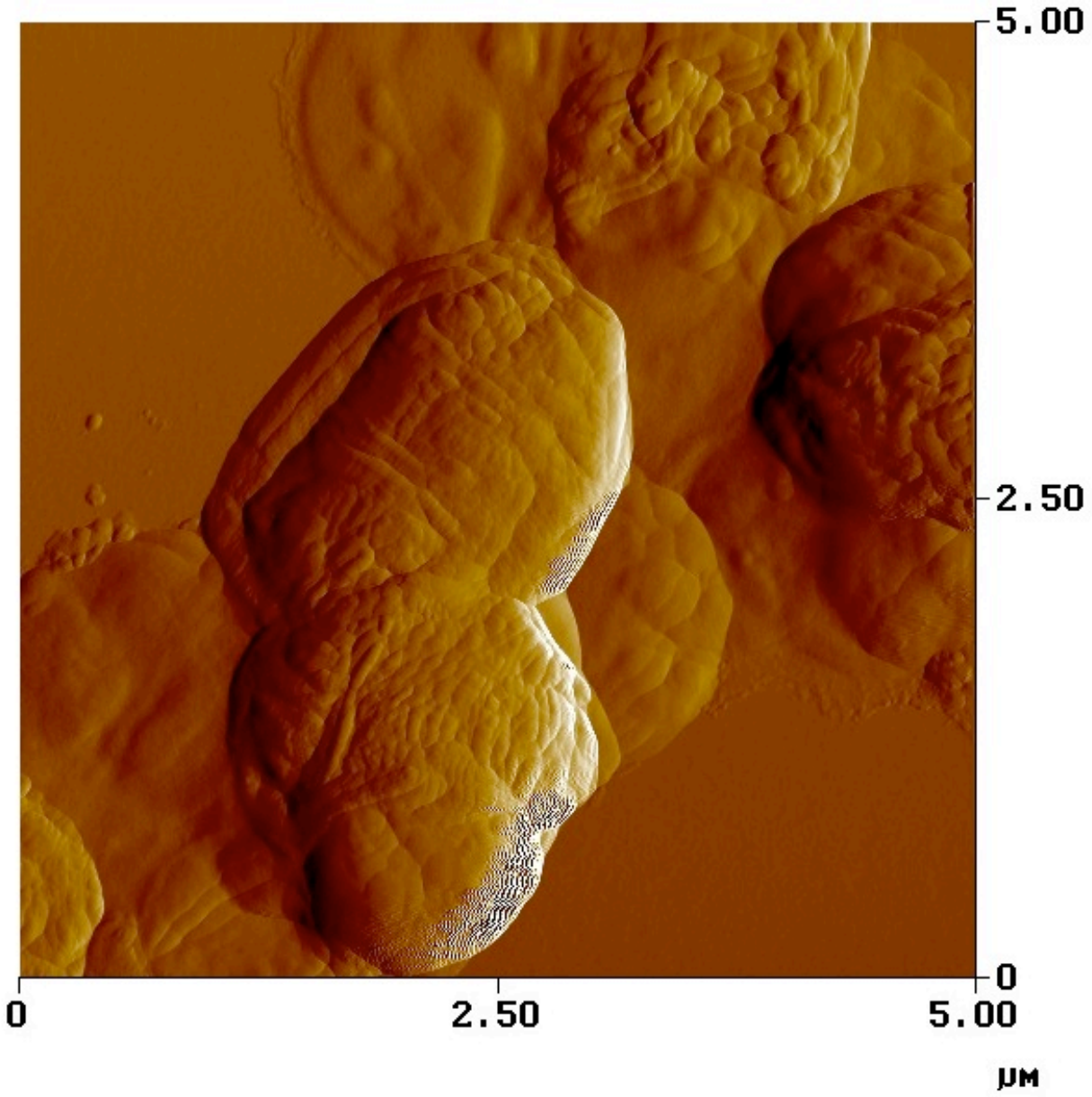
5.00
2.50
0
0
2.50
5.00
µm

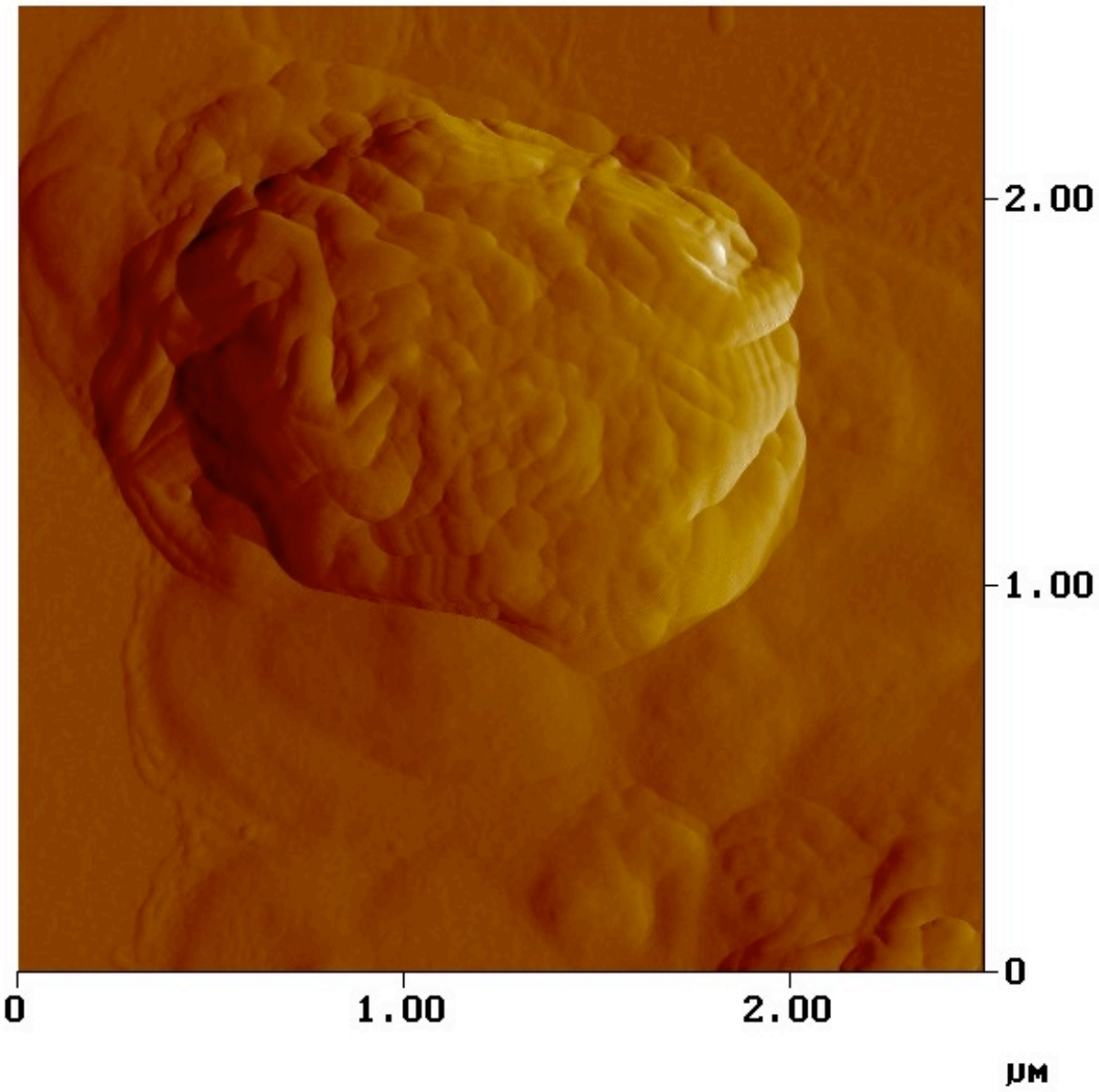
2.00
1.00
0
0
1.00
2.00
µm

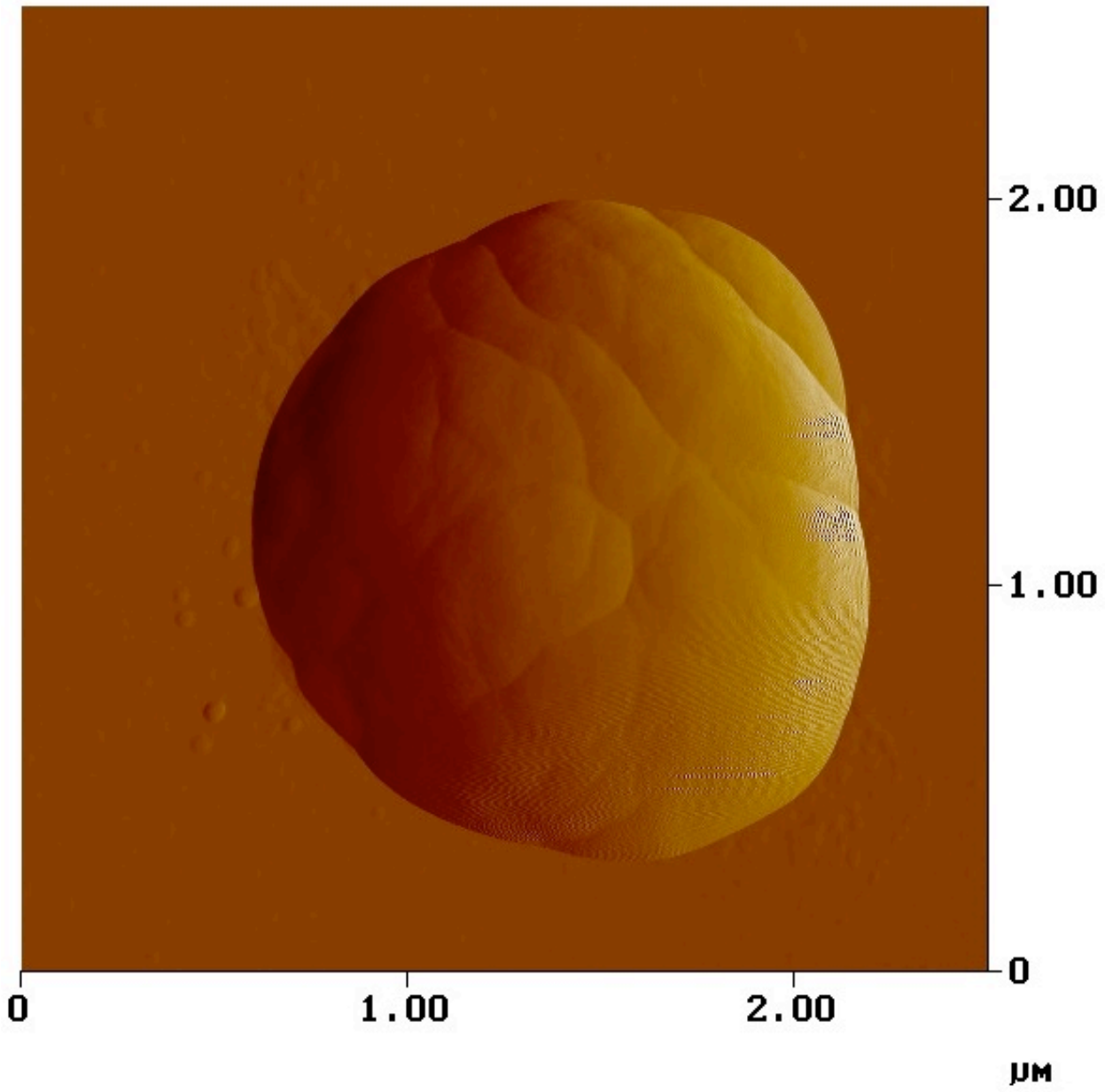
2.00
1.00
0
0
1.00
2.00
µm

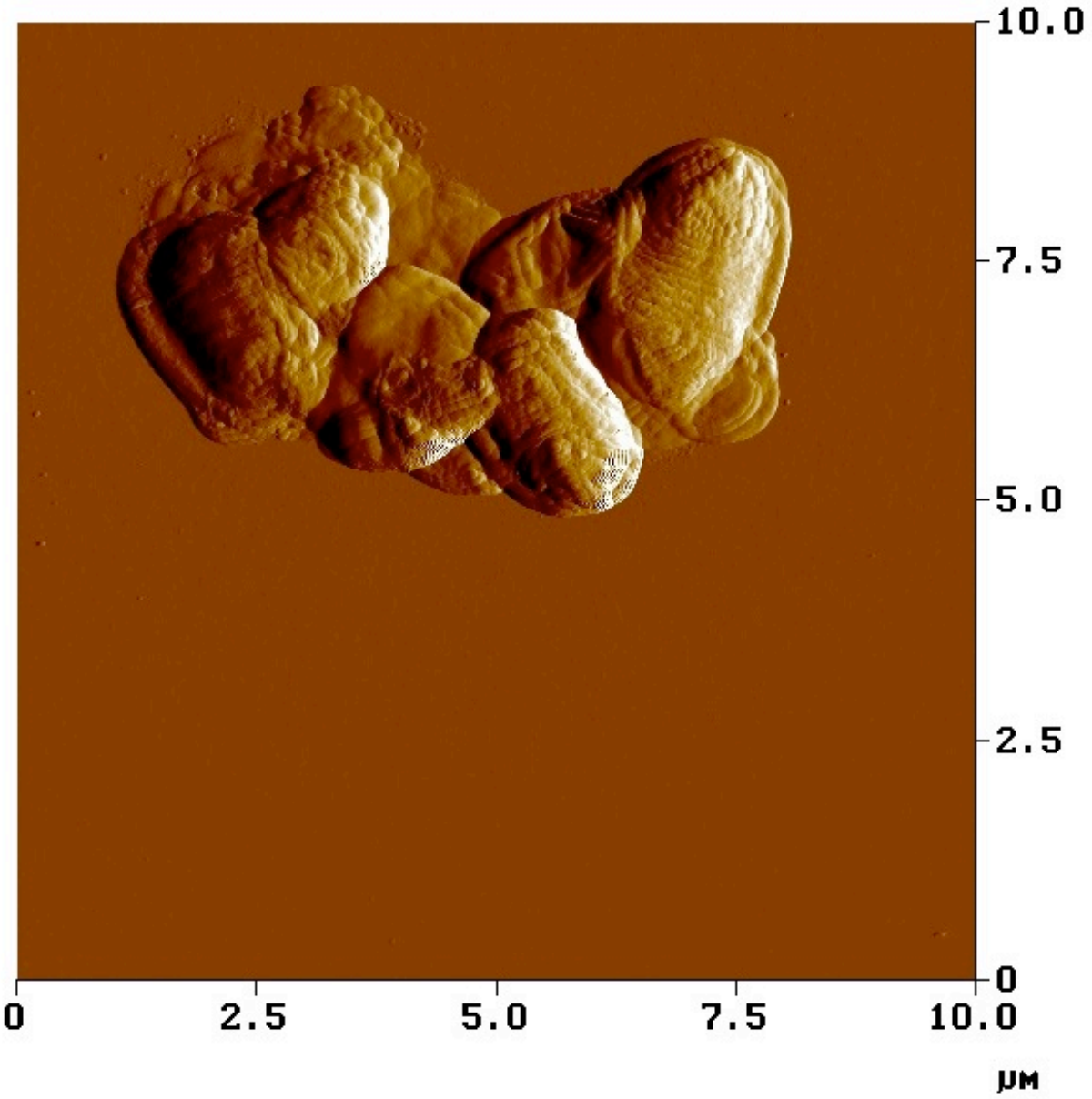
10.0
7.5
5.0
2.5
0
0
2.5
5.0
7.5
10.0
µm

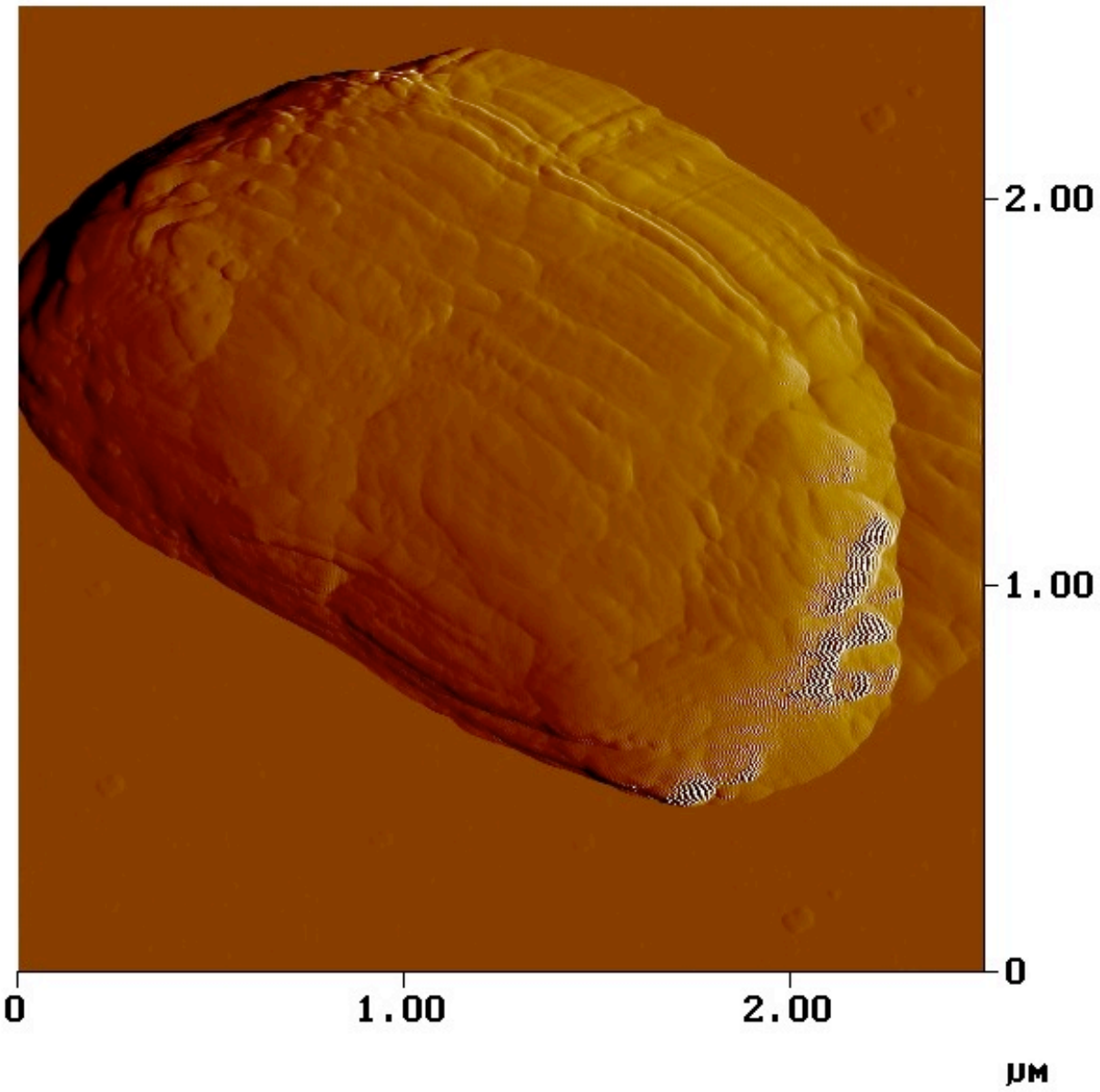
2.00
1.00
0
0
1.00
2.00
µm

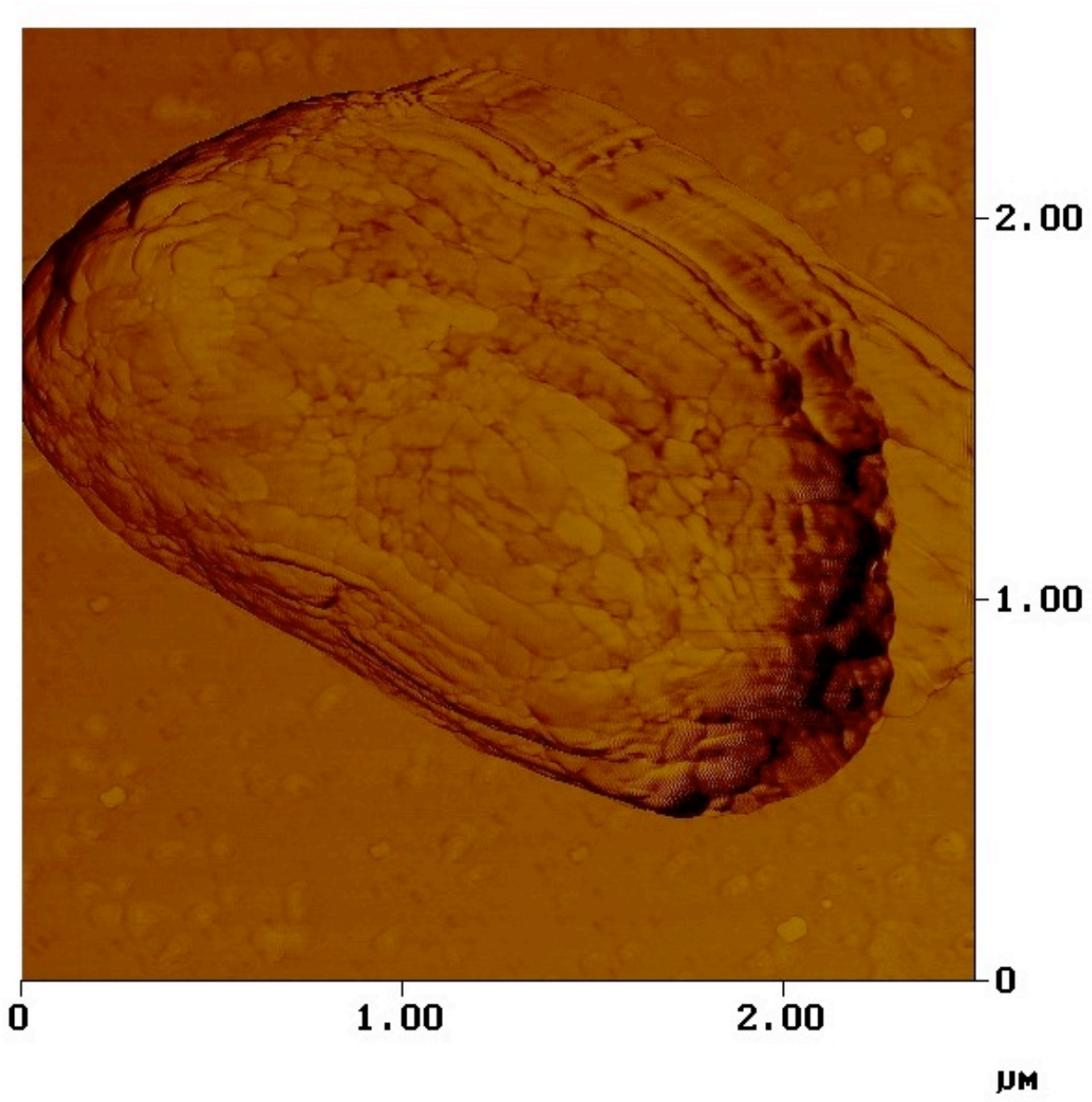

Phase Image

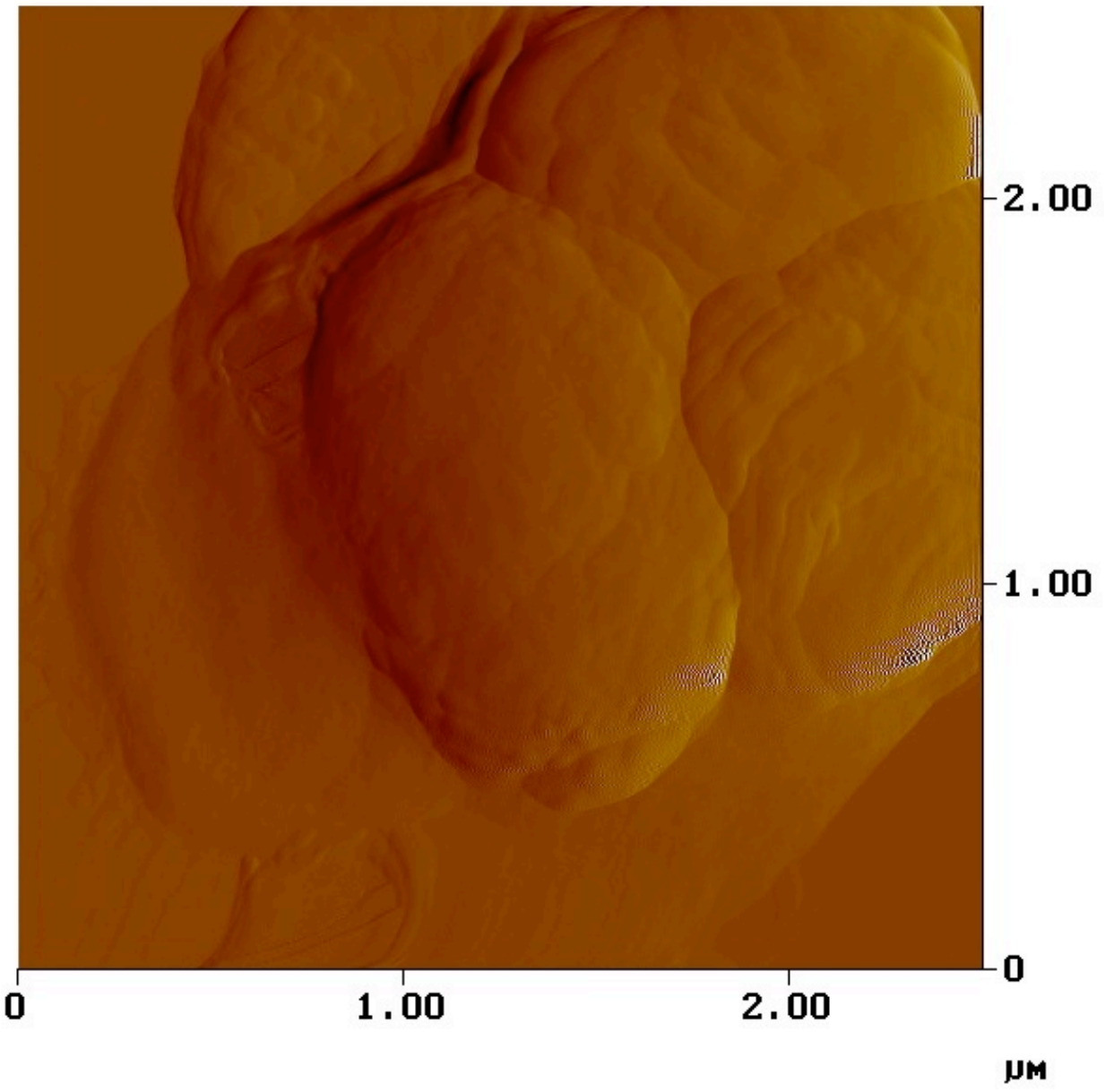

This is another example of how imaging conditions can greatly affect the detail and quality of an image.

APPENDIX E – CELL GEOMETRY AND ROUGHNESS

Sample	Scan Area	Image Number	Length	Width	Area	Height	RMS Roughness
Control	10	1	0.898	0.683	0.613	0.563	
Control	10	1	1.035	0.664	0.687	0.570	
Control	10	1	1.484	0.465	0.690	0.614	15.8
Control	10	1	0.937	0.761	0.713	0.584	
Control	10	1	1.211	0.859	1.040	0.563	
Control	10	1	1.094	0.976	1.068	0.673	12.2
Control	10	1	1.348	0.800	1.078	0.774	7.1
Control	10	1	1.094	1.055	1.154	0.618	17.5
Control	10	1	1.523	0.761	1.159	0.688	
Control	10	1	1.387	0.839	1.164	0.822	12.8
Control	10	1	1.426	0.820	1.169	0.781	10.2
Control	10	1	1.582	0.800	1.266	0.708	12.5
Control	10	1	1.621	0.917	1.486	0.848	14.8
Control	10	1	1.582	0.957	1.514	0.901	20.6
Control	10	1	1.602	0.957	1.533	0.811	9.3
Control	10	1	1.816	0.878	1.594	0.842	13.1
Control	10	1	2.148	0.800	1.718	0.844	14.0
Control	10	1	1.465	1.191	1.745	0.883	
Control	10	1	1.875	0.957	1.794	0.856	11.6
Control	10	1	1.816	1.016	1.845	0.923	11.5
Control	10	1	1.934	0.957	1.851	0.876	
Control	10	1	1.953	0.976	1.906	0.886	19.1
Control	10	1	1.797	1.074	1.930	1.075	
Control	10	1	1.992	1.016	2.024	0.877	
Control	10	1	2.031	1.016	2.063	0.831	12.8
Control	10	1	2.363	0.937	2.214	0.827	16.3
Control	5	7	1.807	0.771	1.393	0.746	10.2
Control	5	7	1.748	0.908	1.587	0.791	11.1
Control	5	7	2.256	0.898	2.026	0.743	12.6
Control	5	7	2.217	1.279	2.836	0.774	15.6
Control	5	11	2.157	1.182	2.550	0.794	6.0
Control	2.5	14	2.202	1.089	2.398	0.727	10.4
Control	5	23	2.402	0.927	2.227	0.866	7.1
Control	2.5	24	2.402	0.927	2.227		13.8
Control	2.5	34	1.978	0.996	1.970		9.9
Control	5	52	0.917	0.722	0.662	0.456	12.1
Control	5	52	0.976	0.722	0.705	0.482	11.4
Control	5	52	1.006	0.859	0.864	0.499	5.9
Control	5	52	1.016	0.898	0.912	0.608	14.3
Control	5	52	1.074	0.917	0.985	0.624	5.7
Control	2.5	53	0.854	0.771	0.658	0.371	16.3
Control	2.5	53	0.883	0.791	0.698	0.497	14.1

Sample	Scan Area	Image Number	Length	Width	Area	Height	RMS Roughness
Control	2.5	55	0.932	0.898	0.837	0.471	13.5
Control	2.5	58	1.665	0.854	1.422	0.709	15.1
Control	2.5	61	1.240	1.079	1.338	0.429	14.4
Control	2.5	62	1.909	1.240	2.367	0.633	17.5
Control	2.5	63	1.157	1.021	1.181	0.414	7.5
Control	2.5	64	1.162	0.747	0.868	0.571	12.4
Control	2.5	64	1.924	1.133	2.180	0.750	10.4
Alanine	5	78	2.715	1.895	5.145	0.614	12.5
Alanine	5	82	3.447	1.904	6.563	0.596	9.3
Alanine	5	83	2.861	1.865	5.336	0.760	8.8
Alanine	5	84	2.627	2.529	6.644	1.059	14.5
Alanine	5	90	2.148	2.100	4.511	0.674	6.2
Inosine	2.5	92	1.733	1.548	2.683	0.646	9.9
Inosine	5	94	1.445	1.250	1.806	0.467	4.8
Inosine	5	94	1.553	1.348	2.093	0.508	4.2
Inosine	2.5	95	1.772	1.587	2.812	0.424	6.1
Inosine	2.5	96	1.406	1.372	1.929	0.351	8.1
Inosine	2.5	97	1.758	1.709	3.004	0.509	4.9
Inosine	5	98	1.660	1.270	2.108	0.514	9.5
Inosine	2.5	99	1.479	1.406	2.079	0.537	9.1
Inosine	2.5	102	1.421	1.323	1.880	0.354	9.5
Alan+Ino	2.5	103	2.070	1.514	3.134	0.298	7.7
Alan+Ino	5	104	2.285	1.572	3.592	0.388	6.4
Alan+Ino	5	106	1.563	1.240	1.938	0.349	6.8
Alan+Ino	2.5	107	1.699	1.685	2.863	0.453	7.9
Alan+Ino	5	108	2.285	1.270	2.902	0.400	6.2
Alan+Ino	5	108	2.266	1.328	3.009	0.437	6.9
Alan+Ino	5	108	2.969	1.387	4.118	0.367	5.8
Alan+Ino	5	110	2.441	1.572	3.837	0.612	8.6
Alan+Ino	2.5	112	1.655	0.942	1.559	0.518	7.3
Inosine	5	114	1.172	0.996	1.167	0.491	6.7
Inosine	5	114	1.211	1.006	1.218	0.572	8.2
Inosine	5	114	1.270	0.966	1.227	0.605	6.5
Inosine	5	114	1.357	0.927	1.258	0.585	6.8
Inosine	5	114	1.211	1.074	1.301	0.498	6.0
Inosine	5	114	1.299	1.104	1.434	0.570	7.2
Inosine	5	114	1.377	1.104	1.520	0.485	6.6
Inosine	5	114	1.279	1.230	1.573	0.552	7.2
Inosine	5	114	1.377	1.260	1.735	0.535	8.6
Inosine	5	114	1.465	1.367	2.003	0.495	6.7